# *Ab initio* calculation of two-photon absorption in semiconductors

Alan Bernal Ramírez and Bernardo S. Mendoza[*]

*Centro de Investigaciones en Óptica, León, 37150 Guanajuato, México*

A theoretical derivation of two-photon absorption (2PA) from semiconductors, based on the length gauge analysis and the electron density operator, is formulated; the *intraband* $\boldsymbol{r}_i$ part and the *interband* $\boldsymbol{r}_e$ part of the position operator $\boldsymbol{r}$ are properly accounted for. Within the independent-particle approximation, the nonlinear third-order susceptibility tensor $\chi^{\mathrm{abcd}}(-\omega; -\omega, -\omega, \omega)$ and the two-photon absorption coefficient are calculated, including the scissors correction needed to correct the well-known underestimation of the local-density-approximation band gap. Using time-reversal symmetry, it is shown that the expression for $\chi^{\mathrm{abcd}}(-\omega; -\omega, -\omega, \omega)$ is finite at $\omega = 0$, avoiding nonphysical divergences presented in previous calculations when $\omega \to 0$. *Ab initio* band structure calculations using different pseudopotential schemes that include spin-orbit coupling are used to calculate the 2PA for several semiconductors, and the calculations are compared with available experimental results for photon energies that are below the optical band gap.

## I. INTRODUCTION

Since the development of the two-photon absorption (2PA) theory in 1931 by Göppert-Mayer [1], a new field of research has emerged. These new optical phenomena opened the gate to better understand optical processes and to develop potential technologies based on 2PA. In this sense, there are current technologies related to 2PA phenomena, such as two-photon excitation microscopy [2] and multiphoton microfabrication and lithography [3–5]; also, work on applications such as optical power limiting [6], optical data storage [7,8], or two-photon photodynamic therapy [9] is being done, as well as research on bioimaging using materials at the nanoscale [10,11]. For this, it is mandatory to conduct experimental and theoretical research on 2PA phenomena in materials; in particular, the explanation and prediction of the microscopic third-order optical response in materials are theoretical targets.

Related to the experimental point of view of 2PA, there are diverse factors that contribute to the difficulty in characterizing materials in the nonlinear regime. Third-order nonlinear susceptibility related to 2PA is obtained through the measurement of nonlinear absorption in materials, and several variables are involved in these kinds of experiments, such as laser-pulse duration and repetition rate, peak power, laser coherence, the presence of free carriers, and competition between nonlinear and linear absorption phenomena, which increases the complexity of material characterization. Hence reported values for the 2PA coefficient are only within a narrow region of the light spectrum and are often varied over orders of magnitude [12], and even more, experimental work only reports the 2PA coefficient instead of the imaginary part of third-order 2PA susceptibility; to our knowledge, only

Furey *et al.* [13] have reported the value of all independent nonzero components of the imaginary part of 2PA susceptibility tensors for GaAs, GaP, and Si in the vicinity of the half band gap for each material. The complex measurement of 2PA third-order susceptibility motivates theoretical investigation of this phenomenon.

To theoretically describe nonlinear optical responses at the microscopic scale and, in specific, to describe 2PA, a lot of research has been done. Hutchings and Van Stryland [14] calculated the 2PA coefficient in zinc-blende semiconductors by means of the Kane band structure model; such a calculation is a more comprehensive study than the two-band model used by Aversa *et al.* to describe 2PA [15]. Additionally, Hutchings and Wherrett [16] first calculated the polarization dependence of 2PA by means of the four-band Kane band structure model and later calculated the anisotropy parameter, including the influence of higher conduction bands, by using the Luttinger-Kohn band structure model [17]. The band structure models cited have the disadvantage of being semiempirical approximations and of describing the absorption phenomena in a vicinity near the center of the Brillouin zone, with a limited number of electronic bands. Alternatively, Aversa and Sipe [18] have cemented the formalism to obtain linear and nonlinear optical responses based on the perturbation theory under the length gauge analysis and the electron density operator. This formalism allowed the accurate calculation of nonlinear optical responses, such as the second-harmonic generator (SHG) [19], and they also suggested computing higher-order optical responses. Related to *ab initio* 2PA calculations, to our knowledge, only Murayama and Nakayama [20–22] have presented *ab initio* full-band-structure calculations; they presented the two-photon absorption spectra and anisotropy of GaAs, ZnSe, and Si using the density-matrix theory, and nonlocal corrections to the local momentum operator and a correction to the self-energy were presented. These calculations have the

[*]bms@cio.mx

disadvantage of presenting apparent unphysical divergences in the infrared regime.

The theoretical derivation of 2PA microscopic susceptibility is presented in this paper under the *ab initio* perturbative model in the independent-particle approximation using a full-band model. This work uses the length gauge approximation as the perturbative interaction between materials and light to obtain the imaginary part of the third-order nonlinear susceptibility, which describes third-order nonlinear absorption. The well-known band-gap underestimation in density functional theory with the local-density approximation (DFT-LDA) is corrected at the scissors operator level, and the inclusion of the spin-orbit coupling (SOC) is taken into account. Also, we show that the unphysical divergences are analytically demonstrated to be zero when $\omega \to 0$, which was not considered in previous *ab initio* calculations; moreover, the $2\omega$ and $1\omega$ terms of $\chi^{\text{abcd}}(-\omega; -\omega, -\omega, \omega)$ are analyzed to obtain a complete third-order optical response, where the position matrix elements are distinguished in the *intraband* $\mathbf{r}_i$ part and the *interband* $\mathbf{r}_e$ part [18,23,24]; this differentiation allows us to disregard nonsignificant terms in $\chi^{\text{abcd}}(-\omega; -\omega, -\omega, \omega)$.

The rest of this paper is organized as follows: Sec. II describes the theoretical derivation of third-order nonlinear susceptibility, Sec. III presents the evaluation of the 2PA coefficient for semiconductors and discusses the results, and Sec. V summarizes our main findings.

## II. THEORY

In this section, we present the scheme used to calculate the third-order nonlinear response $\chi^{\text{abcd}}(-\omega; -\omega, -\omega, \omega)$ using the length gauge formalism, within the independent-particle approach. Some detail is given, since it is important to distinguish between the so-called *intraband* and *interband* transitions. In Appendix A, we show all the steps of the perturbation approach taken, and, in particular, we show how, through time-reversal invariance, the expression for $\chi^{\text{abcd}}(-\omega; -\omega, -\omega, \omega)$ is divergence-free at $\omega = 0$. We mention that the expression for $\chi^{\text{abcd}}(-\omega; -\omega, -\omega, \omega)$ presented in Ref. [21] diverges at $\omega = 0$.

### A. Two-photon absorption

The absorption of two photons of the same frequency is characterized through the third-order nonlinear polarization, written as

$$\mathbf{P}(t) = \epsilon_0 X^{(3)} \mathbf{E}^3(t), \tag{1}$$

where the tensorial character of susceptibility $X^{(3)}$ is suppressed for convenience, and the perturbing electric field $\mathbf{E}(t)$ is given by

$$\mathbf{E}(t) = \mathbf{E}_+(\omega)e^{-i\tilde{\omega}t} + \mathbf{E}_-(\omega)e^{i\tilde{\omega}t}, \tag{2}$$

where $\mathbf{E}_+(\omega) = E(\omega)\hat{\boldsymbol{\varepsilon}}$ and $\mathbf{E}_-(\omega) = E(\omega)\hat{\boldsymbol{\varepsilon}}^*$. Then, $E(\omega)$ gives the magnitude and $\hat{\boldsymbol{\varepsilon}}$ gives the polarization of the electric field. For linear polarization $\hat{\boldsymbol{\varepsilon}} = \hat{\boldsymbol{\varepsilon}}^*$, but for elliptical polarization, $\hat{\boldsymbol{\varepsilon}}$ will have an opposite helicity to $\hat{\boldsymbol{\varepsilon}}^*$. Also, $\tilde{\omega} = \omega + i\eta$, and $\eta = 0^+$ adiabatically switches on the interaction with the electric field. At the end of the calculation, we take $\eta \to 0$. The above field is such that $\mathbf{E}_+(\omega)e^{-i\tilde{\omega}t}$ induces the absorption

of a photon with energy $\hbar\omega$, whereas $\mathbf{E}_-(\omega)e^{i\tilde{\omega}t}$ induces the emission of a photon with energy $\hbar\omega$. Then,

$$\begin{aligned} \mathbf{P}(t) = \epsilon_0 X^{(3)} (&\mathbf{E}_+(\omega)\mathbf{E}_+(\omega)\mathbf{E}_+(\omega)e^{-i3\tilde{\omega}t} \\ &+ 3\mathbf{E}_+(\omega)\mathbf{E}_+(\omega)\mathbf{E}_-(\omega)e^{-i\tilde{\omega}t} \\ &+ 3\mathbf{E}_+(\omega)\mathbf{E}_-(\omega)\mathbf{E}_-(\omega)e^{i\tilde{\omega}t} \\ &+ \mathbf{E}_-(\omega)\mathbf{E}_-(\omega)\mathbf{E}_-(\omega)e^{i3\tilde{\omega}t}), \end{aligned} \tag{3}$$

where the two-photon absorption (2PA) is given by

$$\mathbf{P}(t) = 3\epsilon_0 X^{(3)} \mathbf{E}_+(\omega)\mathbf{E}_+(\omega)\mathbf{E}_-(\omega)e^{-i\tilde{\omega}t}, \tag{4}$$

where two photons, each of frequency $\omega$, are simultaneously absorbed through $\mathbf{E}_+(\omega)$, and the resulting polarization oscillates at $\omega$. The above equation leads to

$$P^{\text{a}}(\omega) = 3\epsilon_0 \chi^{\text{abcd}}(-\omega; -\omega, -\omega, \omega)E_+^{\text{b}}(\omega)E_+^{\text{c}}(\omega)E_-^{\text{d}}(\omega), \tag{5}$$

with $\chi^{\text{abcd}}(-\omega; -\omega, -\omega, \omega)$ being the degenerate third-order nonlinear optical susceptibility tensor describing a polarization density response at the same frequency as the incident frequency [25]. Thus, $\chi^{\text{abcd}}(-\omega; -\omega, -\omega, \omega)$ describes 2PA, whose units are $m^2/V^2$. The roman superscripts denote Cartesian components, where we use the Einstein convention for repeated indices, and $\epsilon_0$ is the vacuum permittivity.

### B. Perturbation approach

In order to derive the analytic expression for the 2PA susceptibility of Eq. (5), we assume that electrons may be described through an independent-particle approximation, although we do allow for many-body effects through an effective Hamiltonian that depends on all the occupied states, as in density functional theory. The electrons interact with an electromagnetic field, which we assume is a classical field. Thus we describe quantum mechanical matter interacting with classical fields. We neglect the local fields and excitonic effects [26], and we write the one-electron Hamiltonian

$$\hat{H}(t) = \hat{H}_0 + \hat{\mathcal{H}}(t) \tag{6}$$

as the sum of an unperturbed effective time-independent Hamiltonian $\hat{H}_0$ that describes the interaction of an electron with the crystalline lattice and its effective interaction with the other electrons, as well as an interaction Hamiltonian $\hat{\mathcal{H}}(t)$, which describes the interaction of the electron with a time-dependent electromagnetic field. We mention that $\hat{H}_0$ includes the scissors operator that allows for the energy correction of the pseudopotentials gap $E_g$ to the experimental energy of the gap $E_{\text{expt}}$ [27]. We describe the state of the system through the one electron density operator $\hat{\rho}$, with which we can calculate the expectation value of any single-particle observable $\hat{\mathcal{O}}$ as $\langle \hat{\mathcal{O}} \rangle = \text{Tr}(\hat{\rho}\hat{\mathcal{O}})$ with Tr denoting the trace. Within the interaction picture ($I$), the density operator evolves in time due to the interaction Hamiltonian according to

$$i\hbar \frac{d}{dt}\hat{\rho}_I(t) = [\hat{\mathcal{H}}_I(t), \hat{\rho}_I(t)], \tag{7}$$

while the operators that correspond to all observables evolve through $\hat{H}_0$ according to

$$\hat{\mathcal{O}}_I(t) = \hat{U}^\dagger(t)\hat{\mathcal{O}}(t)\hat{U}(t), \tag{8}$$

where $\hat{\mathcal{O}}(t)$ is the same observable in the Schrödinger picture, given by $\hat{\mathcal{O}}(0)$ for operators that do not depend explicitly on time, and

$$\hat{U}(t) = \exp(-i\hat{H}_0 t/\hbar) \qquad (9)$$

is the nonperturbed unitary time-evolution operator. Assuming that the field is turned on adiabatically, we may integrate (7) to yield

$$\hat{\rho}_I(t) = \hat{\rho}_{I0} + \frac{1}{i\hbar} \int_{-\infty}^{t} dt' [\hat{\mathcal{H}}_I(t'), \hat{\rho}_I(t')], \qquad (10)$$

where $\hat{\rho}_{I0}$ is the unperturbed, time-independent equilibrium density matrix. We look for the standard perturbation series solution, $\hat{\rho}_I(t) = \hat{\rho}_{I0} + \hat{\rho}_I^{(1)}(t) + \hat{\rho}_I^{(2)}(t) + \cdots$, where the superscript denotes the order (power) with which each term depends on perturbation $\hat{\mathcal{H}}_I(t)$. The $(N + 1)$th-order solution is given as

$$\hat{\rho}_I^{(N+1)}(t) = \frac{1}{i\hbar} \int_{-\infty}^{t} dt' [\hat{\mathcal{H}}_I(t'), \hat{\rho}_I^{(N)}], \quad N \geqslant 0, \qquad (11)$$

where $\hat{\rho}_I^{(N)}$ is the density matrix of the previous order perturbation term. For 2PA, $N + 1 = 3$, and then, we need to know $\hat{\rho}_I^{(0)}$, $\hat{\rho}_I^{(1)}$, and $\hat{\rho}_I^{(2)}$ to obtain $\hat{\rho}_I^{(3)}$.

We take our system as a solid described by a nonperturbed periodic Hamiltonian, whose eigenfunctions are Bloch states, $|m\mathbf{k}\rangle$, characterized by a band index $m$ and a crystal momentum $\mathbf{k}$. For $\hat{\mathcal{H}}_I(t)$, we take the interaction with an electromagnetic field with a wavelength much larger than the crystal unit cell dimension. Thus electronic transitions due to this interaction are vertical; that is, they conserve $\mathbf{k}$. Taking the matrix elements between Bloch states of Eq. (8), we obtain

$$\langle n\mathbf{k}|\hat{\mathcal{O}}_I|m\mathbf{k}\rangle \equiv \mathcal{O}_{I,nm}(\mathbf{k}, t) = e^{i\omega_{nm}(\mathbf{k})t} \langle n\mathbf{k}|\hat{\mathcal{O}}|m\mathbf{k}\rangle$$
$$= e^{i\omega_{nm}(\mathbf{k})t} \mathcal{O}_{nm}(\mathbf{k}, t), \qquad (12)$$

where $\omega_{nm}(\mathbf{k}) \equiv \omega_n(\mathbf{k}) - \omega_m(\mathbf{k})$ and $E_n(\mathbf{k}) = \hbar\omega_n(\mathbf{k})$ are the unperturbed energy eigenvalues corresponding to the stationary Schrödinger's equation $\hat{H}_0|n\mathbf{k}\rangle = E_n(\mathbf{k})|n\mathbf{k}\rangle$, where the Bloch states $|n\mathbf{k}\rangle$ are chosen so that $\langle \mathbf{r}|n\mathbf{k}\rangle = u_{n\mathbf{k}}(\mathbf{r})e^{i\mathbf{k}\cdot\mathbf{r}}$, with $u_{n\mathbf{k}}(\mathbf{r})$ being cell periodic and $\langle n\mathbf{k}|m\mathbf{k}'\rangle = \delta_{nm}\delta(\mathbf{k} - \mathbf{k}')$.

Within the dipole approximation, the interaction Hamiltonian in the length gauge is given by [27]

$$\hat{\mathcal{H}}_I(t) = -e\hat{\mathbf{r}}_I(t) \cdot \mathbf{E}(t), \qquad (13)$$

where $\hat{\mathbf{r}}_I(t) = \hat{U}_0^\dagger(t)\hat{\mathbf{r}}U(t)$ is the position operator of the electron at time $t$, and from Eq. (2), $\mathbf{E}(t) = \mathbf{E}_\pm(\omega)e^{\mp i\tilde{\omega}t}$, the time-dependent perturbing classical electric field that, as explained in the previous section, induces two-photon absorption through the correct choices of $\mathbf{E}(t)$, as given in Eq. (5). Then, from Eqs. (11) and (12) we obtain

$$\rho_{I,nm}^{(N+1)}(\mathbf{k}, t) = \frac{ie}{\hbar} \int_{-\infty}^{t} dt' e^{i\omega_{nm}(\mathbf{k})t'} \langle n\mathbf{k}|[\hat{\mathbf{r}}, \hat{\rho}^{(N)}]|m\mathbf{k}\rangle \cdot \mathbf{E}(t'),$$
$$(14)$$

where it is convenient to represent the position operator in the coordinate space $\hat{\mathbf{r}} \to \mathbf{r}$ when calculating its *interband* matrix elements, and in the reciprocal space $\hat{\mathbf{r}} \to i\nabla_{\mathbf{k}}$ when calculating its *intraband* matrix elements, so that following Refs. [18,28,29], the matrix elements of **r** are split between

the *intraband* ($\mathbf{r}_i$) and *interband* ($\mathbf{r}_e$) parts, where $\mathbf{r} = \mathbf{r}_i + \mathbf{r}_e$ and

$$\langle n\mathbf{k}|\hat{\mathbf{r}}_i|m\mathbf{k}'\rangle = \delta_{nm}[\delta(\mathbf{k} - \mathbf{k}')\boldsymbol{\xi}_{nn}(\mathbf{k}) + i\nabla_{\mathbf{k}}\delta(\mathbf{k} - \mathbf{k}')], \quad (15)$$

$$\langle n\mathbf{k}|\hat{\mathbf{r}}_e|m\mathbf{k}'\rangle = (1 - \delta_{nm})\delta(\mathbf{k} - \mathbf{k}')\boldsymbol{\xi}_{nm}(\mathbf{k}), \qquad (16)$$

with

$$\boldsymbol{\xi}_{nm}(\mathbf{k}) \equiv i\frac{(2\pi)^3}{\Omega} \int_{\Omega} d\mathbf{r}\, u_{n\mathbf{k}}^*(\mathbf{r})\nabla_{\mathbf{k}} u_{m\mathbf{k}}(\mathbf{r}) \qquad (17)$$

being the Berry connection, where $\Omega$ is the unit cell volume. The well-known commutator

$$\hat{\mathbf{v}} = \dot{\hat{\mathbf{r}}} = \frac{1}{i\hbar}[\hat{\mathbf{r}}, \hat{H}_0] \qquad (18)$$

allows us to write the interband matrix element as

$$\mathbf{r}_{nm}(\mathbf{k}) = \frac{\mathbf{v}_{nm}(\mathbf{k})}{i\omega_{nm}(\mathbf{k})} \quad (n \neq m), \qquad (19)$$

where $\hat{\mathbf{v}}$ is the velocity operator related to the momentum operator by $\hat{\mathbf{p}} = m\hat{\mathbf{v}}$, with m being the mass of the electron. For $\mathbf{r}_e$, we obtain that

$$\langle n\mathbf{k}|[\hat{r}^a, \hat{\rho}^{(N)}(t)]|m\mathbf{k}\rangle = \sum_{\ell \neq m,n} \left(r_{n\ell}^a(\mathbf{k})\rho_{\ell m}^{(N)}(\mathbf{k}, t)\right.$$
$$\left. - \rho_{n\ell}^{(N)}(\mathbf{k}, t)r_{\ell m}^a(\mathbf{k})\right)(1 - \delta_{nm})$$
$$\equiv R_{nm}^{a,(N)}(\mathbf{k}, t), \qquad (20)$$

where we used the closure relationship $\sum_n |n\mathbf{k}\rangle\langle n\mathbf{k}| = 1$. When $\mathbf{r}_i$ appears in commutators, we use

$$\langle n\mathbf{k}|[\hat{r}_i^a, \hat{\rho}^{(N)}(t)]|m\mathbf{k}\rangle = i\rho_{nm;k^a}^{(N)}(\mathbf{k}, t) \equiv R_{i,nm}^{a,(N)}(\mathbf{k}, t) \quad (21)$$

with

$$\rho_{nm;k}^{(N)}(\mathbf{k}, t) = \nabla_{\mathbf{k}}\rho_{nm}^{(N)}(\mathbf{k}, t) - i\rho_{nm}^{(N)}(\mathbf{k}, t)(\boldsymbol{\xi}_{nn}(\mathbf{k}) - \boldsymbol{\xi}_{mm}(\mathbf{k})),$$
$$(22)$$

where ";$\mathbf{k}$" denotes the generalized derivative with respect to $\mathbf{k}$ and $\rho_{nm}^{(N)}(\mathbf{k}, t)$ could be replaced by any function.

From Eq. (14), we obtain

$$\rho_{I,nm}^{(N+1)}(\mathbf{k}, t) = \frac{ie}{\hbar} \int_{-\infty}^{t} dt' e^{i(\omega_{nmk} \pm \tilde{\omega}_p)t'}$$
$$\times \left[R_{nm}^{b,(N)}(\mathbf{k}, t') + R_{i,nm}^{b,(N)}(\mathbf{k}, t')\right]E_{\mp}^b(\omega_p), \quad (23)$$

where subscript $p$ is a tag to keep track of the frequency $\omega_p$ that belongs to the Cartesian direction b.

The perturbation series is generated by the unperturbed density operator

$$\langle n\mathbf{k}|\hat{\rho}^{(0)}|m\mathbf{k}\rangle = \delta_{nm}f(\hbar\omega_n(\mathbf{k})) \equiv f_n(\mathbf{k}), \qquad (24)$$

with $f_n(\mathbf{k})$ being the Fermi-Dirac distribution; for a clean, cold semiconductor, $f_n(\mathbf{k}) = 1$ when $n$ is a valence ($v$) or occupied band, and $f_n(\mathbf{k}) = 0$ when $n$ is a conduction ($c$) or empty band. This defines the distribution functions $f_n(\mathbf{k})$ in reciprocal space, one for each band. Also, following Ref. [18], we can readily show that

$$\langle n\mathbf{k}|[\hat{\mathbf{r}}, \hat{\rho}^{(0)}]|m\mathbf{k}\rangle = f_{mn}(\mathbf{k})\mathbf{r}_{nm}(\mathbf{k}) + i\delta_{nm}\nabla_{\mathbf{k}}f_n(\mathbf{k}), \qquad (25)$$

where $f_{nm}(\mathbf{k}) = f_n(\mathbf{k}) - f_m(\mathbf{k})$. For a clean, cold semiconductor, $\nabla_{\mathbf{k}}f_n(\mathbf{k}) = 0$, and thus there are no intraband contributions

to the optical response; however, this term is finite for metallic systems and gives rise to their low-frequency optical behavior through the so-called Drude tensor [30]. From Eq. (20), $R^{a,(0)}_{nm}(\boldsymbol{k}, t) = f_{mn}(\boldsymbol{k})r^a_{nm}(\boldsymbol{k})(1 - \delta_{nm})$, and from Eq. (21), $R^{a,(0)}_{i,nm}(\boldsymbol{k}, t) = 0$, which, when used in Eq. (23), leads to $\rho^{(1)}_{I,nm}(\boldsymbol{k}, t) = e^{i\omega_{nm}(\boldsymbol{k})t}\rho^{(1)}_{nm}(\pm\omega_p, t)$, where

$$\rho^{(1)}_{nm}(\pm\omega_p, \boldsymbol{k}, t) = B^b_{nm}(\pm\omega_p, \boldsymbol{k})(1 - \delta_{nm})E^b_{\mp}(\omega_p)e^{\pm i\tilde{\omega}_p t}, \tag{26}$$

with

$$B^b_{nm}(\pm\omega_p, \boldsymbol{k}) = \frac{e}{\hbar}\frac{f_{mn}(\boldsymbol{k})r^b_{nm}(\boldsymbol{k})}{\omega_{nm}(\boldsymbol{k}) \pm \tilde{\omega}_p}. \tag{27}$$

For the linear response, $\rho^{(1)}_{nm}(-\omega_p, \boldsymbol{k}, t)$ $[\rho^{(1)}_{nm}(+\omega_p, \boldsymbol{k}, t)]$ would lead to the absorption (emission) of a photon with energy $\hbar\omega_p$.

We proceed with the second-order terms, and from Eqs. (20) and (21) we obtain

$$R^{b(1)}_{e,nm}(\boldsymbol{k}, t) = \frac{e}{\hbar}\sum_{\ell\neq m,n}\left(r^b_{n\ell}(\boldsymbol{k})B^c_{\ell m}(\boldsymbol{k}, \pm\omega_q)\right.$$
$$\left. - B^c_{n\ell}(\boldsymbol{k}, \pm\omega_q)r^b_{\ell m}(\boldsymbol{k})\right)(1 - \delta_{nm})E^c_{\mp\omega_q}e^{\pm i\tilde{\omega}_q t} \tag{28}$$

and

$$R^{b(1)}_{i,nm}(\boldsymbol{k}, t) = \frac{ie}{\hbar}B^c_{nm;k^b}(\boldsymbol{k}, \pm\omega_q)(1 - \delta_{nm})E^c_{\mp\omega_q}e^{\pm i\tilde{\omega}_q t}, \tag{29}$$

where we use $\omega_q$ to differentiate it from $\omega_p$, since it is associated with the electrical field along the Cartesian direction c. From Eq. (23), we obtain that $\rho^{(2)}_{I,nm}(\boldsymbol{k}, t) = e^{i\omega_{nm}(\boldsymbol{k})t}\rho^{(2)}_{nm}(\pm\tilde{\omega}_p \pm \tilde{\omega}_q, \boldsymbol{k}, t)$, where $\rho^{(2)}_{nm}(\pm\omega_p \pm \omega_q, \boldsymbol{k}, t) = \rho^{(2)}_{nm}(\pm\omega_p \pm \omega_q, \boldsymbol{k})E^b_{\mp p}E^c_{\mp q}e^{i(\pm\tilde{\omega}_p \pm \tilde{\omega}_q)t}$, with

$$\rho^{(2)}_{nm}(\pm\omega_p \pm \omega_q, \boldsymbol{k}) = \frac{e^2}{\hbar^2}\frac{1}{\omega_{nm\boldsymbol{k}} \pm \tilde{\omega}_p \pm \tilde{\omega}_q}\left[iB^c_{nm;k^b}(\pm\omega_q, \boldsymbol{k})\right.$$
$$\left. + \sum_{\ell\neq nm}\left(r^b_{n\ell}B^c_{\ell m}(\pm\omega_q, \boldsymbol{k}) - B^c_{n\ell}(\pm\omega_q, \boldsymbol{k})r^b_{\ell m}\right)\right](1 - \delta_{nm}). \tag{30}$$

We mention that the above expression would lead to second-harmonic generation by taking $-\omega_q = -\omega_p = -\omega$ [27,31].

Finally, we proceed with the third-order nonlinear response. Then, from Eqs. (20) and (21),

$$R^{d(2)}_{e,nm}(\boldsymbol{k}, t) = \sum_{\ell\neq nm}\left(r^d_{n\ell}(\boldsymbol{k})\rho^{(2)}_{\ell m}(\pm\omega_p \pm \omega_q, \boldsymbol{k}) - \rho^{(2)}_{n\ell}(\pm\omega_p \pm \omega_q, \boldsymbol{k})r^d_{\ell m}(\boldsymbol{k})\right)E^b_{\mp p}E^c_{\mp q}e^{i(\pm\omega_p \pm \omega_q - i\eta)t}(1 - \delta_{nm}), \tag{31}$$

and

$$R^{d(2)}_{i,nm}(\boldsymbol{k}, t) = i\rho^{(2)}_{nm;k^d}(\pm\omega_p \pm \omega_q, \boldsymbol{k})E^b_{\mp p}E^c_{\mp q}(1 - \delta_{nm})e^{i(\pm\omega_p \pm \omega_q - i\eta)t}. \tag{32}$$

Then, from Eq. (23), $\rho^{(3)}_{I,nm}(\boldsymbol{k}, t) = e^{i\omega^\Sigma_{nm\boldsymbol{k}}t}\rho^{(3)}_{nm}(\pm\omega_p \pm \omega_q \pm \omega_s, \boldsymbol{k}, t)$, where

$$\rho^{(3)}_{nm}(\pm\omega_p \pm \omega_q \pm \omega_s, \boldsymbol{k}, t) = \rho^{(3)}_{nm}(\pm\omega_p \pm \omega_q \pm \omega_s, \boldsymbol{k})E^d_{\mp s}E^b_{\mp p}E^c_{\mp q}e^{i(\pm\omega_p \pm \omega_q \pm \omega_s - i\eta)t} \tag{33}$$

and

$$\rho^{(3)}_{nm}(\pm\omega_p \pm \omega_q \pm \omega_s, \boldsymbol{k}) = \frac{e}{\hbar}\left[\sum_{\ell\neq nm}\left(r^d_{n\ell}(\boldsymbol{k})\rho^{(2)}_{\ell m}(\pm\omega_p \pm \omega_q, \boldsymbol{k}) - \rho^{(2)}_{n\ell}(\pm\omega_p \pm \omega_q, \boldsymbol{k})r^d_{\ell m}(\boldsymbol{k})\right)\right.$$
$$\left. + i\rho^{(2)}_{nm;k^d}(\pm\omega_p \pm \omega_q, \boldsymbol{k})\right]\frac{1 - \delta_{nm}}{\omega_{nm}(\boldsymbol{k}) \pm \tilde{\omega}_p \pm \tilde{\omega}_q \pm \tilde{\omega}_s}, \tag{34}$$

where now $\omega_s$ is associated with the Cartesian direction d of the electric field.

From Eq. (5), 2PA is given by this combination of fields, $E^b_+(\omega)E^c_+(\omega)E^d_-(\omega)$, which in turn implies that $\omega_p = -\omega, \omega_q = -\omega$, and $\omega_s = \omega$, so that from Eq. (34), the third-order density matrix that describes 2PA is given by

$$\rho^{(3)}_{nm}(-\omega, \boldsymbol{k}) = \frac{e}{\hbar}\sum_{\ell\neq mn}\left[\left(r^d_{n\ell}(\boldsymbol{k})\rho^{(2)}_{\ell m}(-2\omega, \boldsymbol{k}) - \rho^{(2)}_{n\ell}(-2\omega, \boldsymbol{k})r^d_{\ell m}(\boldsymbol{k})\right) + i\rho^{(2)}_{nm;k^d}(-2\omega, \boldsymbol{k})\right]\frac{1 - \delta_{nm}}{\omega_{nm}(\boldsymbol{k}) - \omega}, \tag{35}$$

where, from Eq. (30),

$$\rho^{(2)}_{nm}(-2\omega, \boldsymbol{k}) = \frac{e^2}{\hbar^2}\frac{\mathcal{G}^{bc}_{nm}(-\omega, \boldsymbol{k})}{\omega_{nm}(\boldsymbol{k}) - 2\tilde{\omega}} \tag{36}$$

with

$$\mathcal{G}^{bc}_{nm}(-\omega, \boldsymbol{k}) = iB^c_{nm;k^b}(-\omega, \boldsymbol{k}) + \sum_{\ell\neq mn}\left(r^b_{n\ell}(\boldsymbol{k})B^c_{\ell m}(-\omega, \boldsymbol{k}) - B^c_{n\ell}(-\omega, \boldsymbol{k})r^b_{\ell m}(\boldsymbol{k})\right), \tag{37}$$

and $B^c_{nm}(-\omega, \boldsymbol{k})$ is given in Eq. (27), with the generalized derivative "$;\boldsymbol{k}$" in Eq. (22).

### C. 2PA susceptibility

To obtain the 2PA response, we look for the expectation value of the macroscopic polarization density $\boldsymbol{P}$, whose time derivative yields the current density $\boldsymbol{J}$ as

$$\frac{\partial}{\partial t}\boldsymbol{P} = \boldsymbol{J} = \frac{e}{\Omega}\mathrm{Tr}(\hat{\boldsymbol{v}}\hat{\rho}^{(3)}(t)), \tag{38}$$

where $\Omega$ is the volume of the unit cell, from Eq. (33),

$$\boldsymbol{P}(\omega) = \frac{ie}{\omega}\int\frac{d\boldsymbol{k}}{8\pi^3}\sum_{mn}\boldsymbol{v}_{mn}(\boldsymbol{k})\rho_{nm}^{(3)}(-\omega,\boldsymbol{k})E_+^{\mathrm{b}}E_+^{\mathrm{c}}E_-^{\mathrm{d}}, \tag{39}$$

and using Eq. (5), we obtain that

$$\chi^{\mathrm{abcd}}(-\omega;-\omega,-\omega,\omega) = \frac{ie^2}{\hbar\omega}\int\frac{d\boldsymbol{k}}{8\pi^3}\sum_{m\neq n}v_{mn}^{\mathrm{a}}(\boldsymbol{k})\left[\sum_{\ell\neq mn}\left(r_{n\ell}^{\mathrm{d}}(\boldsymbol{k})\rho_{\ell m}^{(2)}(-2\omega,\boldsymbol{k}) - \rho_{n\ell}^{(2)}(-2\omega,\boldsymbol{k})r_{\ell m}^{\mathrm{d}}(\boldsymbol{k})\right)\right.$$
$$\left. + i\rho_{nm;k^{\mathrm{d}}}^{(2)}(-2\omega,\boldsymbol{k})\right]\frac{1}{\omega_{nm}(\boldsymbol{k}) - \tilde{\omega}} \tag{40}$$

is the third-order nonlinear susceptibility that describes 2PA in semiconductors; integration over $\boldsymbol{k}$ is over the Brillouin zone (BZ). In Appendix A, we show how to obtain explicit expressions for $\chi^{\mathrm{abcd}}(-\omega;-\omega,-\omega,\omega)$ that we use to calculate 2PA. Those expressions are composed of terms that resonate when the external frequency of the incoming beam of light $\hbar\omega \geqslant E_{\mathrm{gap}}$ or $\hbar\omega \geqslant E_{\mathrm{gap}}/2$, where $E_{\mathrm{gap}}$ is the energy gap of the semiconductor. We mention that the factor of 3 that appears in Eq. (5) is the factor of 3 that is given in the numerator of Eq. (44) as obtained in Ref. [13].

In this paper, we are mainly interested in 2PA for $E_{\mathrm{gap}}/2 \leqslant \hbar\omega < E_{\mathrm{gap}}$, which, according to Appendix A, would correspond to the $2\omega$ expression for $\chi^{\mathrm{abcd}}(-\omega;-\omega,-\omega,\omega)$ given in Eqs. (A18), (A22), (A32), and (A35), so that

$$\mathrm{Im}[\chi_{2\omega}^{\mathrm{abcd}}] = \frac{\pi e^4}{\hbar^3}\int\frac{d\boldsymbol{k}}{8\pi^3}\sum_{vc}\left(\frac{16\Delta_{cv}^{\mathrm{d}}(\boldsymbol{k})\mathrm{Im}[r_{cv;k^{\mathrm{b}}}^{\mathrm{c}}(\boldsymbol{k})v_{vc}^{\mathrm{a}}(\boldsymbol{k})]}{\omega_{cv}^4(\boldsymbol{k})} - \frac{32\Delta_{cv}^{\mathrm{b}}(\boldsymbol{k})\Delta_{cv}^{\mathrm{d}}(\boldsymbol{k})\mathrm{Im}[v_{vc}^{\mathrm{a}}(\boldsymbol{k})r_{cv}^{\mathrm{c}}(\boldsymbol{k})]}{\omega_{cv}^5(\boldsymbol{k})}\right.$$
$$\left. - \frac{8\mathrm{Im}[v_{vc;k^{\mathrm{d}}}^{\mathrm{a}}(\boldsymbol{k})r_{cv;k^{\mathrm{b}}}^{\mathrm{c}}(\boldsymbol{k})]}{\omega_{cv}^3(\boldsymbol{k})} + \frac{16\Delta_{cv}^{\mathrm{b}}(\boldsymbol{k})\mathrm{Im}[r_{cv}^{\mathrm{c}}(\boldsymbol{k})v_{vc;k^{\mathrm{d}}}^{\mathrm{a}}(\boldsymbol{k})]}{\omega_{cv}^4(\boldsymbol{k})}\right)\delta(\omega_{cv}(\boldsymbol{k}) - 2\omega), \tag{41}$$

where we have suppressed the argument $(-\omega;-\omega,-\omega,\omega)$ to save space; the generalized derivatives of $v_{nm;k^b}^a(\boldsymbol{k})$ and $r_{nm;k^b}^a(\boldsymbol{k})$ are given in Eqs. (A6) and (A7), respectively. It is worth mentioning that the expression involves transitions only from valence ($v$) to conduction ($c$) states. Indeed, as it turns out, the terms of $\chi_{2\omega}^{\mathrm{abcd}}(-\omega;-\omega,-\omega,\omega)$ that have summations that involve three and four energy states (Appendix A) are $10^5$ times smaller than what Eq. (41) gives; therefore we could ignore them throughout this paper. Finally, as described in Ref. [27], the scissors operator would lead to the following modifications:

$$\omega_n^{\Sigma}(\boldsymbol{k}) = \omega_n^{\mathrm{LDA}}(\boldsymbol{k}) + (1 - f_n(\boldsymbol{k}))\Sigma, \tag{42}$$

with $\omega_n^{\mathrm{LDA}}(\boldsymbol{k})$ being the LDA energy of band $n$ at point $\boldsymbol{k}$ and $\Sigma$ being the energy or "scissors shift" required to obtain the experimental energy gap of the semiconductor in question. Also,

$$\boldsymbol{v}_{nm}^{\Sigma}(\boldsymbol{k}) = \boldsymbol{v}_{nm}^{\mathrm{LDA}}(\boldsymbol{k}) + i\Sigma f_{nm}(\boldsymbol{k})\boldsymbol{r}_{nm}(\boldsymbol{k}) \tag{43}$$

gives the scissor shift to the velocity matrix elements.

To summarize the procedure used to obtain the 2PA susceptibility, in Fig. 1 we show a tree diagram of the electronic density $\rho_{i,e}^{(N)}$ and its intraband $\boldsymbol{r}_i$ and interband $\boldsymbol{r}_e$ contributions to every order in the perturbation scheme presented above. As mentioned before, for a clean, cold semiconductor, $\nabla_{\boldsymbol{k}}f_n(\boldsymbol{k}) =$

0, and there are no intraband contributions to $\rho_i^{(1)}$, for which the left branch of Fig. 1 vanishes; however, this branch is finite for a metal. On the other hand, the right branch of the tree is always finite for both semiconductors and metals. As shown in Sec. III, the contributions from three bands and four bands to 2PA are negligible with respect to the contributions from two bands, which is why the only contributing term to 2PA susceptibility is the branch circled in the tree, and it corresponds to $\rho_{eii}^{(3)}$, which involves "one" contribution from $\boldsymbol{r}_e$ and "two" from $\boldsymbol{r}_i$. Indeed, in Eqs. (A49)–(A52) we identify each of the contributions of the last right branch of Fig. 1 given by $\rho_{eii}^{(3)}$, $\rho_{eie}^{(3)}$, $\rho_{eei}^{(3)}$, and $\rho_{eee}^{(3)}$. As we show in Sec. III, $\rho_{eii}^{(3)}$ dominates the 2PA response for the semiconductors used in this paper.

### III. RESULTS

The self-consistent ground state and the Kohn-Sham states were calculated in the DFT framework using the plane-wave ABINIT code [32]. In what follows, we calculate the results for 2PA using different pseudopotentials within several approximations, in order to determine which scheme gives the best results. For LDA, we used Troullier-Martins pseudopotentials [33] that are fully separable nonlocal pseudopotentials in the Kleinman-Bylander form [34] [LDA with norm-conserving pseudopotentials (LDA-PSPNC)]. To include the spin-orbit
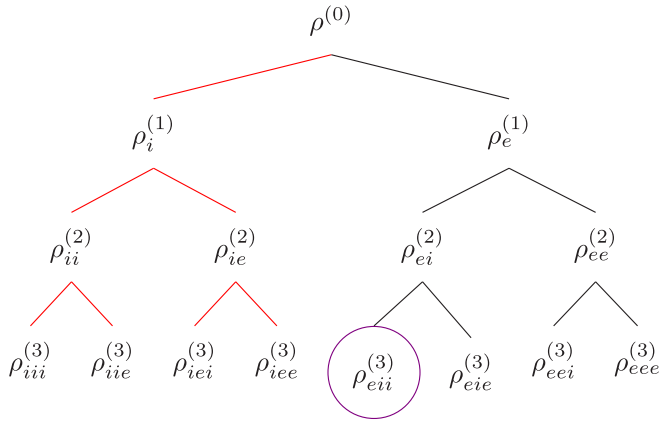
FIG. 1. Tree diagram of the electronic density $\rho_{i,e}^{(N)}$ and its intraband $\boldsymbol{r}_i$ and interband $\boldsymbol{r}_e$ contributions to every order in the perturbation scheme presented in Sec. II B. The $\rho_{eii}^{(3)}$, $\rho_{eie}^{(3)}$, $\rho_{eei}^{(3)}$, and $\rho_{eee}^{(3)}$ are given in Eqs. (A49)–(A52), respectively. The only contributing term to 2PA susceptibility of the tree is the term $\rho_{eii}^{(3)}$, circled in violet, which is composed of only two-band transitions. The $\rho_{eie}^{(3)}$, $\rho_{eei}^{(3)}$, and $\rho_{eee}^{(3)}$ branches are related to three- and four-band transitions, and although finite, they are negligible, as shown in Sec. III. For a semiconductor, the left branch of the tree in red vanishes identically.



FIG. 2. $\mathrm{Im}[\chi_{2\omega}^{xxyy}]$ for GaAs using the different sets of pseudopotentials described in the text. $E_g = 1.424$ eV is the experimental energy gap of GaAs, and $E_g/2$ is half the gap where 2PA becomes finite. No spin-orbit coupling is used in these results.

coupling (SOC) effect, we used Hartwigsen-Goedecker-Hutter (HGH) relativistic separable dual-space Gaussian pseudopotentials (LDA-HGH) [35]. To go beyond the LDA approximation, we use the generalized-gradient approximation (GGA) [36,37] and the meta-GGA (mGGA) [38].

We used 58 415 $\boldsymbol{k}$-points in order to have well-converged results for the irreducible Brillouin zone (IBZ) integration, as given in Eq. (41), using the linear analytic tetrahedron method of Ref. [39]. Also, a cutoff energy of 24 hartrees was used for the plane waves, and nine conduction bands ($c$) were used for the summations in Eq. (41). BeTe, diamond, GaP, GaAs, GaSb, Ge, InAs, InSb, Si CdTe, ZnS, and ZnSe have eight valence bands ($v$); all the semiconductors have been studied with their corresponding experimental lattice constant $a_0$ and band-gap $E_g$, as shown in Appendix B for a non-SOC calculation (Table II) and for a SOC calculation (Table III). For GaAs, Si, and GaP, there are experimental data with which we compare our theoretical results, and we discuss them in detail; for all the other semiconductors mentioned above we only present the 2PA spectra as obtained within the SOC approach.

We start by comparing the results for $\chi_{2\omega}^{abcd}(-\omega; -\omega, -\omega, \omega)$, using the several pseudopotential schemes described in the first paragraph of this section. All the semiconductors studied in this paper are fcc, and thus the only components that are different from zero due to their cubic $F$-43$m$ space group are the $xxyy$, $xyyx$, and $xxxx$ components (and the cyclic $x \to y \to z$ change). From here on, we suppress the $(-\omega; -\omega, -\omega, \omega)$ argument for ease of presentation. We chose only the $xxyy$ component as an example; on the one hand, it gives the largest value for $\chi_{2\omega}^{abcd}$, and on the other hand it conveys the same conclusions that the $xxxx$ and $xyyx$ components lead to. We chose GaAs, since the 2PA for this semiconductor has been recently measured [13], and it is a representative example of all
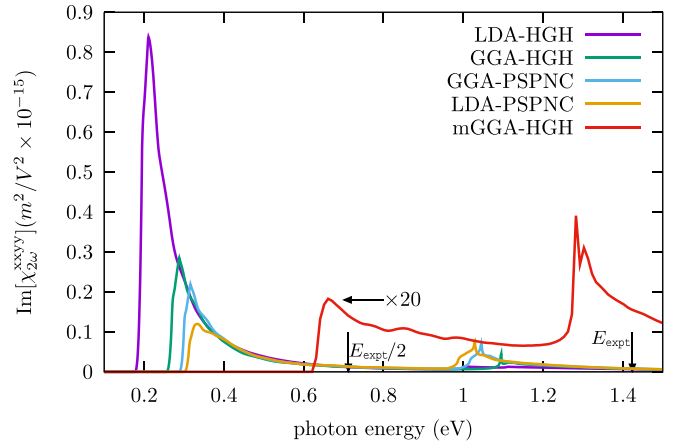
the semiconductors used in this paper. In Fig. 2, we show $\mathrm{Im}[\chi_{2\omega}^{xxyy}]$ vs the photon energy ($\hbar\omega$) for GaAs using the LDA-HGH, GGA-HGH, GGA-PSPNC, LDA-PSPNC, and mGGA-HGH. This sequence of pseudopotentials goes from the highest to the smallest magnitude of $\mathrm{Im}[\chi_{2\omega}^{xxyy}]$. The energy value where $\mathrm{Im}[\chi_{2\omega}^{xxyy}]$ is abruptly finite corresponds to $E_g/2$; as expected then, $\mathrm{Im}[\chi_{2\omega}^{xxyy}]$ shows first a very well defined resonant peak and then other resonances that are below $E_g$. Also, the theoretical value of $E_g/2$ for each approach increases towards the experimental 2PA gap $E_{\mathrm{expt}}/2$. Indeed, we see that for mGGA-HGH, the 2PA gap $E_g/2 = 0.617$ eV is very similar to the experimental value of $E_{\mathrm{expt}}/2 = 0.707$ eV. As we see from Table II of Appendix B, the mGGA-HGH gaps are much closer to the experimental values than the LDA gaps are. We also notice that the magnitude of $\mathrm{Im}[\chi_{2\omega}^{xxyy}]$ for mGGA-HGH is much smaller than for the other pseudopotentials. Due to the fact that mGGA-HGH gives the best energy gap $E_g$, in the following results we only use these pseudopotentials to calculate 2PA. In this section, we present the results without the inclusion of the SOC effect, leaving its inclusion to Sec. IV A.

In Fig. 3, we show $\mathrm{Im}[\chi^{abcd}]$ as a function of $\hbar\omega$, where the $2\omega$ response is different from zero just at $E_g/2$ as expected and then it goes through a maximum and decreases as $\hbar\omega$ approaches $E_g$. Also, we see that $\mathrm{Im}[\chi_{2\omega}^{xxxx}]$ and $\mathrm{Im}[\chi_{2\omega}^{xxyy}]$ are positive, whereas $\mathrm{Im}[\chi_{2\omega}^{xyyx}]$ is negative below $E_g$. In the same figure, we only show $\mathrm{Im}[\chi_{1\omega}^{xxxx}]$, as it is the largest of the three components related to $1\omega$ resonances, as explained in Appendix A, in particular, in Eqs. (A47) and (A48). We see that $\mathrm{Im}[\chi_{1\omega}^{xxxx}]$ is finite around $E_g$, as it must be, and although it is a factor of 2 larger than $\mathrm{Im}[\chi_{2\omega}^{abcd}]$, $\mathrm{Im}[\chi_{1\omega}^{abcd}]$, it does not contribute to 2PA below the gap $E_g$, which makes it unnecessary in this paper.

As is well known, the pseudopotential schemes underestimate the energy gap $E_g$, as clearly seen in Fig. 2. To correct this deficiency within the scissors approximation, one needs to apply the scissors shift, as prescribed in Eqs. (42) and (43). For GaAs, a value of $\Sigma = 0.189$ eV is required to bring the mGGA-HGH gap to 1.424 eV, which is the experimental value
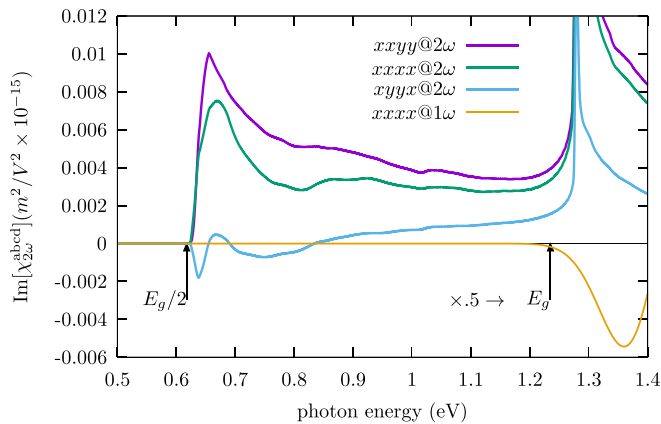
FIG. 3. $\text{Im}[\chi_{2\omega}^{abcd}]$ for GaAs, where we see that the $2\omega$ response starts at $E_g/2$, while the $1\omega$ response starts at $E_g = 1.235$ eV, which is the mGGA gap.

at room temperature. We mention that this value of $\Sigma$ is rather small as compared with what would be needed for the other pseudopotential schemes presented in Fig. 2. In Fig. 4, we show $\text{Im}[\chi_{2\omega}^{abcd}]$ for the nonscissored case, i.e., $\Sigma = 0$, and the scissored case of $\Sigma = 0.189$ eV. Both spectra are roughly the same, as if the scissors correction rigidly shifted the spectra from lower energies to higher energies; however, the scissors operator also lowers the intensity of the 2PA susceptibility by a factor of $\sim 0.73$. In Sec. IV, where the theoretical 2PA absorption is compared with experimental results, it is shown that the scissors correction yields the correct experimental values.

Equation (A48) shows all the terms that contribute to $\chi_{p\omega}^{abcd}$, where $p = 1$ refers to the $1\omega$ processes that are different from zero above the gap and thus, as explained before, are of no interest for this work. For $p = 2$, we get the $2\omega$ processes that are finite below the gap, where $\chi_{1,1,2\omega}^{abcd}$, $\chi_{1,2,2\omega}^{abcd}$, $\chi_{2,1,2\omega}^{abcd}$, $\chi_{2,2,2\omega}^{abcd}$ are the terms that contribute the most to $\chi_{2\omega}^{abcd}$ and which all come from transitions between two bands only. Indeed, the terms that
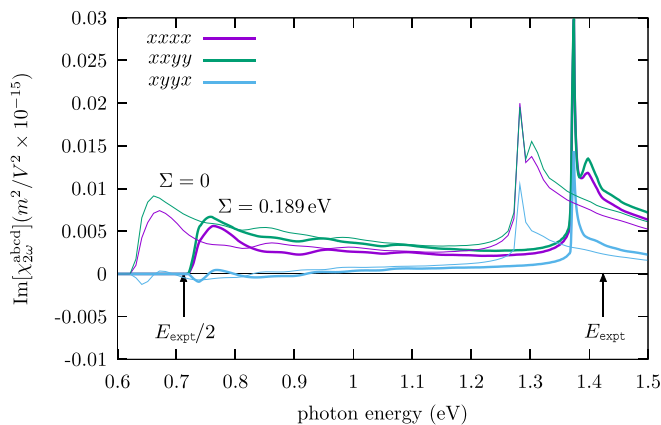


FIG. 4. $\text{Im}[\chi_{2\omega}^{abcd}]$ for GaAs, with and without the contribution of the scissors operator. The experimental gap of GaAs at room temperature is 1.424 eV, and with $\Sigma = 0.189$ eV, it is enough to get the 2PA susceptibility to the experimental $E_{\text{expt}}/2$.
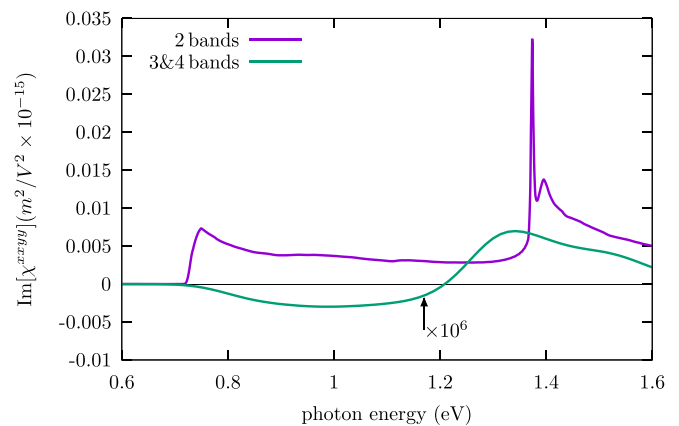


FIG. 5. $\text{Im}[\chi_{2\omega}^{xyy}]$ for GaAs corresponding to transitions of two bands, and $\text{Im}[\chi_{3\&4}^{xyy}]$ corresponding to transitions among three bands and four bands. The latter is smaller by a factor of $10^{-6}$.

involve transitions among three bands and four bands are negligible, as shown in Fig. 5, where we show $\chi_{2\omega}^{xyy} = \chi_{1,1,2\omega}^{xyy} + \chi_{1,2,2\omega}^{xyy} + \chi_{2,1,2\omega}^{xyy} + \chi_{2,2,2\omega}^{xyy}$, corresponding to two bands, and $\chi_{3\&4}^{xyy} = \chi_{1,3,2\omega}^{xyy} + \chi_{2,3,2\omega}^{xyy} + \chi_{3,1,2\omega}^{xyy} + \chi_{3,2,2\omega}^{xyy} + \chi_{3,3,1,2\omega}^{xyy} + \chi_{3,3,2,2\omega}^{xyy} + \chi_{4,1,2\omega}^{xyy} + \chi_{4,2,2\omega}^{xyy} + \chi_{4,3,1,2\omega}^{xyy} + \chi_{4,3,2,2\omega}^{xyy}$, corresponding to three bands and four bands; there, we see that these terms are a factor of $10^{-6}$ smaller, and therefore they can be neglected. We mention that calculating these terms takes a factor of $\approx 300$ times longer than the calculation of $\chi_{2\omega}^{abcd}$; the latter takes $\approx 210$ min in 64 cores of an Intel processor for $\approx 58\,415\boldsymbol{k}$ points, which gives well-converged results for the IBZ integration, as given in Eq. (41). Therefore the fact that $\chi_{3\&4}^{xyy}$ is negligible eases the burden of numerical calculation.

## IV. COMPARISON WITH EXPERIMENTS

In Ref. [13], the 2PA of GaAs, GaP, and Si was experimentally measured using femtosecond pump-probe modulation spectroscopy. For GaAs, which is a direct-gap semiconductor, the measurements were done for photon energies $\hbar\omega$ such that $E_g/2 < \hbar\omega < E_g$, where $E_g$ is the gap energy of GaAs. For GaP, which is an indirect-gap semiconductor, the measurements were done for photon energies $\hbar\omega$ such that $E_g/2 < \hbar\omega < E_g$, where $E_g$ is the direct-gap energy of GaP. However, for Si, which is also an indirect-gap semiconductor, the measurements were done only for photon energies $\hbar\omega$ such that $E_g^i/2 < \hbar\omega < E_g^i$, where $E_g^i$ is the indirect-gap energy of Si. Therefore, for such photon energies, the indirect transitions are most likely due to phonon-assisted processes, and since our theoretical framework only considers direct transitions, it does not apply to this experimental situation. Nevertheless, we use the results for Si of Ref. [40] that were measured for photon $\hbar\omega$ such that $E_g/2 < \hbar\omega < E_g$, with $E_g$ being the direct-gap energy of Si.

2PA is characterized by a pump-probe $\beta_{11}^{\|}$ coefficient, where $\|$ indicates the copolarized beams used in the experiment and the subscript 11 means that the two photons have the same energy. As explained in Ref. [13], after solving the nonlinear wave equation on a plane-wave basis under the slowly varying field amplitude approximation, for a monochromatic

and linearly polarized incident field, one gets a relation between the 2PA $\beta_{11}^{\parallel}$ coefficient and the imaginary part of the third-order nonlinear susceptibility, as follows:

$$\beta_{11}^{\parallel}(\omega) = \frac{3\omega}{2\epsilon_0 n^2(\omega)c^2}\text{Im}\left[\chi_{2\omega}^{XXXX}\right], \qquad (44)$$

where $\chi_{2\omega}^{XXXX}$ is given in the $XYZ$ laboratory coordinate system. Indeed, in the experiments, the beams propagate along $Z = 110$ in crystallographic coordinates, with $X = \bar{1}10$ and $Y = 001$, which defines a basis of linear polarization directions. Therefore we have to rotate $\chi_{2\omega}^{abcd}$ to the crystallographic coordinates by applying the following rotation:

$$\chi_{2\omega}^{ABCD} = \mathcal{R}_A^a \mathcal{R}_B^b \mathcal{R}_C^c \mathcal{R}_D^d \chi_{2\omega}^{abcd}, \qquad (45)$$

using the rotation matrix that applies to the experimental conditions of Ref. [13], i.e.,

$$\mathcal{R} = \begin{bmatrix} -\cos\theta & \cos\theta & \sqrt{2}\sin\theta \\ \sin\theta & -\sin\theta & \sqrt{2}\cos\theta \\ 1 & 1 & 0 \end{bmatrix}, \qquad (46)$$

where $\theta$ is the sample rotation angle in order to express Eq. (44) in terms of $\chi_{2\omega}$ tensor components in crystallographic coordinates. This enables us to take advantage of the $\bar{4}3m$ (GaP and GaAs) or $m3m$ (Si) crystal symmetry, for which there are only three independent, nonvanishing components, $\chi_{2\omega}^{aaaa}$, $\chi_{2\omega}^{aabb} = \chi_{2\omega}^{abab}$, and $\chi_{2\omega}^{abba}$, where a $\neq$ b. Then [13],

$$\beta_{11}^{\parallel}(\omega) = \frac{3\omega\text{Im}\left[\chi_{2\omega}^{xxxx}(\omega)\right]}{32\epsilon_o n^2(\omega)c^2}((3\cos(4\theta) - 4\cos(2\theta) - 7)\sigma(\omega) + 16), \qquad (47)$$

and

$$\sigma(\omega) = 1 - \frac{2\text{Im}\left[\chi_{2\omega}^{xxyy}\right] + \text{Im}\left[\chi_{2\omega}^{xyyx}\right]}{\text{Im}\left[\chi_{2\omega}^{xxxx}\right]} \qquad (48)$$

is known as the anisotropy parameter, with $\theta$ being the sample rotation angle, which, from Ref. [13], is equal to zero. Thus the three independent components of $\text{Im}[\chi_{2\omega}^{abcd}]$ of a $\bar{4}3m$ or $m3m$ crystal contribute to the measurement of two-beam 2PA while rotating the sample about $Z = 110$ in copolarized geometry. Finally, $n(\omega) = \sqrt{\epsilon(\omega)}$ is the index of refraction with $\epsilon(\omega)$ being the dielectric function, which for the $\bar{4}3m$ and $m3m$ crystal symmetries $\epsilon(\omega) = \epsilon^{xx}(\omega) = \epsilon^{yy}(\omega) = \epsilon^{zz}(\omega)$.

In Fig. 6, we show the convergence of $\beta_{11}^{\parallel}(\omega)$ as a function of the number of $\boldsymbol{k}$ points required for the integration over the IBZ. We mention that as seen in Eqs. (47) and (48), $\beta_{11}^{\parallel}(\omega)$ depends on $\chi_{2\omega}^{xxxx}$, $\chi_{2\omega}^{xxyy}$, and $\chi_{2\omega}^{xyyx}$ and the index of refraction $n(\omega)$. As it turns out, $n(\omega)$ converges much faster than $\chi_{2\omega}^{abcd}$, and a rather large number of $\boldsymbol{k}$ points are needed in order to get converged results for $\beta_{11}^{\parallel}(\omega)$. As a compromise for the numerical burden, we chose 58 415 $\boldsymbol{k}$ points for the integration over the IBZ of the results shown below.

In Fig. 7, we show $\beta_{11}^{\parallel}(\omega)$ for the different pseudopotential schemes used in this paper, all calculated with 58 415 $\boldsymbol{k}$ points. Just as in Fig. 2, we see a similar spectral shape with the big difference that the result for mGGA-HGH now has the same order of magnitude as the results for the other approaches. This comes from the fact that $\beta_{11}^{\parallel}(\omega)$ is a ratio between $\chi_{2\omega}^{abcd}$ and $n(\omega)$, and $n(\omega)$ is larger for LDA-HGH, GGA-HGH,
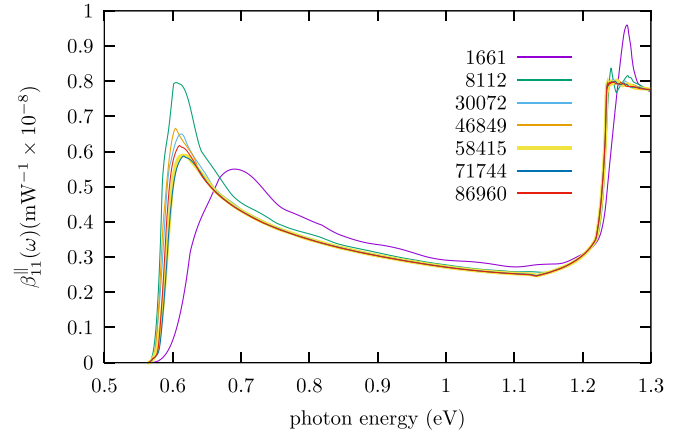


FIG. 6. Convergence of $\beta_{11}^{\parallel}(\omega)$ as a function of the number of $\boldsymbol{k}$ points required for the integration over the IBZ. As a compromise for the numerical burden, we chose 58 415 $\boldsymbol{k}$ points for the calculations.

GGA-PSPNC, and LDA-PSPNC than for mGGA-HGH, thus giving a similar magnitude for $\beta_{11}^{\parallel}(\omega)$.

In Fig. 8, we compare our results of $\beta_{11}^{\parallel}(\omega)$ with the corresponding experimental results of Ref. [13] for GaAs. The theoretical results have $\Sigma = 0.189$ eV, which corresponds to the scissors shift to bring the mGGA-HGH gap to the experimental gap, as given in Table II of Appendix B. We mention that $\Sigma$ shifts 2PA by $\Sigma/2$, since below the gap, only $2\omega$ transitions are finite. As with the results presented in Fig. 4, where the scissors shift lowers the magnitude of $\chi_{2\omega}^{abcd}$, the magnitude of $\beta_{11}^{\parallel}(\omega)$ also decreases as $\Sigma$ increases; in this case, $n(\omega)$ also contributes to this effect, as it also decreases as $\Sigma$ increases, and since $\beta_{11}^{\parallel}(\omega) \propto 1/n^2(\omega)$, as seen from Eq. (47), the overall effect of increasing $\Sigma$ is that $\beta_{11}^{\parallel}(\omega)$ diminishes more than $\chi_{2\omega}^{abcd}$ does. From Fig. 8, we find a reasonable match between the theoretical results and the experimental results, as far as the spectroscopic signature is concerned. To wit, there is a clear maximum in both, and although the width of the 2PA peak is not equal, the theoretical results clearly show a
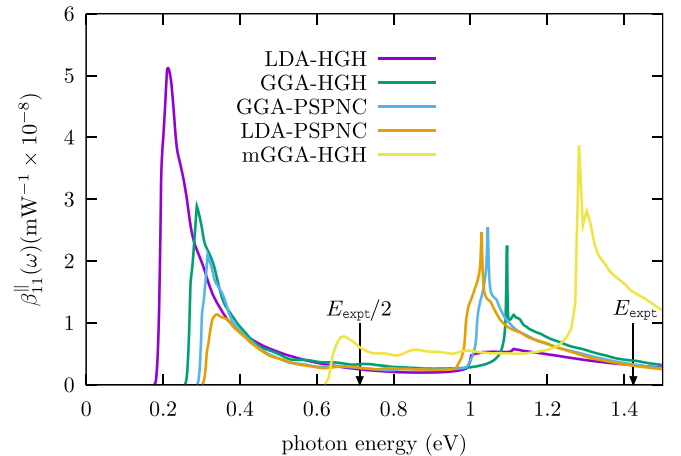


FIG. 7. $\beta_{11}^{\parallel}(\omega)$ for the different pseudopotential schemes used in this paper, calculated with 58 415 $\boldsymbol{k}$ points for the integration over the IBZ.
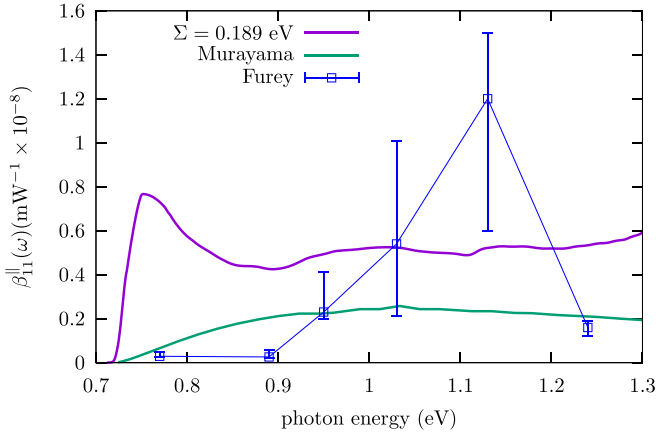
FIG. 8. Theoretical 2PA $\beta_{11}^{\parallel}(\omega)$ coefficient for GaAs vs photon energy, where the scissors shift $\Sigma = 0.189$ eV takes the theoretical gap energy $E_g/2$ of the mGGA-HGH scheme to the experimental value. The theoretical results of Murayama and Nakayama [21] are shown by the green line. The squares are the experimental results for $\beta_{11}^{\parallel}(\omega)$ of Furey *et al.* [13]. See text for details.

resonance in the response. Also, both the experimental and theoretical spectra are of the same order of magnitude for both values of $\Sigma$. In Fig. 8, we also compare our results with the theoretical results of Murayama and Nakayama [21]. We see that the results of Murayama and Nakayama do not present a resonance and are a factor of ~6 smaller than the experimental results. Although the object of this paper is not to analyze why Ref. [21] gives such results, we mention that their expression for Im$[\chi^{\mathrm{abcd}}(-\omega; -\omega, -\omega, \omega)]$ diverges at $\omega = 0$, does not include the *intraband* $\hat{r}_i$ contribution of the $\hat{r}$ position operator, and only presents $\omega$ resonances. We emphasize that from Fig. 1, our expression for $\chi_{2\omega}^{\mathrm{abcd}}$ depends mainly on $\rho_{eii}^{(3)}$, which includes contributions from both $r_i$ and $r_e$, and that below the energy gap $E_g$, only $2\omega$ resonances contribute, in contrast to the expression of Ref. [21]. As shown in Fig. 8, the $2\omega$ resonance qualitatively matches the experimental results.

### A. Spin-orbit coupling effects

In Fig. 9, we show $\beta_{11}^{\parallel}(\omega)$ vs photon energy with and without the inclusions of the spin-orbit coupling (SOC) interaction for GaAs. For this case we have used $\Sigma = 0.65$ eV (with SOC) and $\Sigma = 0.540$ eV (without SOC) as the scissors-shift values needed to bring the theoretical with-SOC and without-SOC results to where the experimental 2PA rises from near-zero values to finite values. We see that the SOC theoretical spectrum shows a small shift to larger photon energies and a larger magnitude, as compared with the result without SOC. The second broad resonance obtained in the result without SOC for $\beta_{11}^{\parallel}(\omega)$ is absent in the result with SOC, and the magnitude of the SOC result is much closer to that of the experimental results shown in the same figure.

In Fig. 10, we compare our 2PA Im$[\chi_{2\omega}^{\mathrm{abcd}}]$ for GaAs including SOC with the experimental results of Ref. [13] and those of Ref. [41]. As we did in Fig. 9, we use $\Sigma = 0.65$ eV to bring the theoretical SOC results to where the experimental 2PA rises from near-zero values to finite values. The results of Ref. [13] give Im$[\chi_{2\omega}^{xxyy}] \approx$ Im$[\chi_{2\omega}^{xxxx}]$, and Im$[\chi_{2\omega}^{xyyx}]$ is
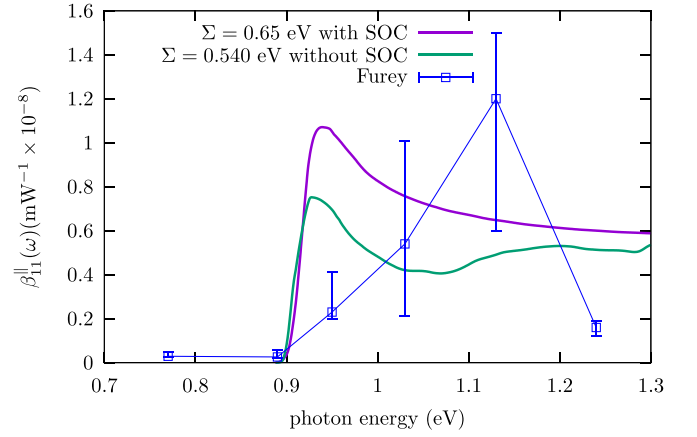


FIG. 9. 2PA GaAs coefficient $\beta_{11}^{\parallel}(\omega)$ vs photon energy with and without the spin-orbit coupling (SOC) effect. The blue squares are the experimental results of Furey *et al.* [13]. See text for details.

smaller, whereas for Ref. [41], the results are only for a photon energy of 1.3 eV, and Im$[\chi_{2\omega}^{xxxx}] >$ Im$[\chi_{2\omega}^{xxyy}] \approx$ Im$[\chi_{2\omega}^{xyyx}]$. The relative size of our theoretical results follows Im$[\chi_{2\omega}^{xxyy}] >$ Im$[\chi_{2\omega}^{xxxx}] >$ Im$[\chi_{2\omega}^{xyyx}]$; then, only Im$[\chi_{2\omega}^{xxyy}]$ and Im$[\chi_{2\omega}^{xyyx}]$ follow the experimental trend of Ref. [13]. We remark that the experimental values of Im$[\chi_{2\omega}^{\mathrm{abcd}}]$ are inferred from the measurement of the $\beta_{11}^{\parallel}$ coefficient, and judging from the experimental error bars, they may not be precise. Finally, we see that the orders of magnitude of the theoretical and experimental values for Im$[\chi_{2\omega}^{\mathrm{abcd}}]$ are similar.

In Fig. 11, we compare our 2PA $\beta_{11}^{\parallel}(\omega)$ results for Si, with and without SOC, with the experimental results $\beta_{\mathrm{eff}}(\omega)$ of Ref. [40]. The values of $\Sigma$ are those required to get the theoretical half gap of Si to its experimental value of 1.7 eV, as given in Table II of Appendix B. Our results show an abrupt rise in $\beta_{11}^{\parallel}(\omega)$ just above $E_{\mathrm{expt}}/2$ and then several resonances. The first one is a strong narrow resonance that starts just above 1.8 eV, rises sharply as the photon energy increases, and then encounters a second sharp resonance, albeit with a smaller intensity; this second resonance is much stronger for the SOC case. Then, around 2.2 eV, both the SOC and the non-SOC
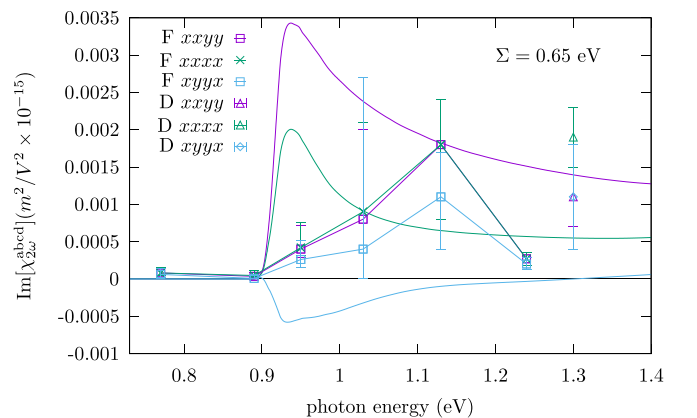


FIG. 10. Theoretical 2PA Im$[\chi_{2\omega}^{\mathrm{abcd}}]$, including SOC for GaAs, compared with the experimental results of Furey *et al.* [13] (F) and Dvorak *et al.* [41] (D). See text for details.
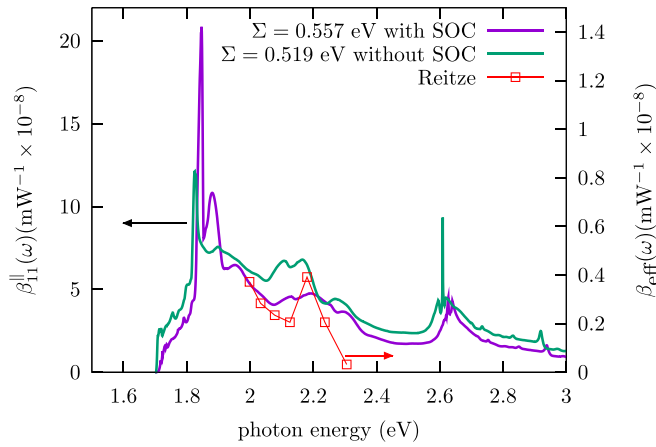
FIG. 11. Theoretical $\beta_{11}^{\parallel}(\omega)$ (left axis) and experimental $\beta_{\text{eff}}(\omega)$ (right axis) 2PA coefficient for Si vs $\hbar\omega$, where the red squares are the experimental results of Reitze *et al.* [40]. See text for details.
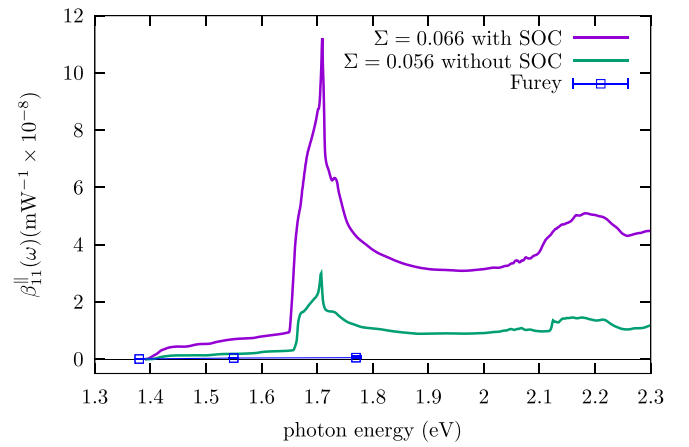


FIG. 12. Theoretical and experimental $\beta_{11}^{\parallel}(\omega)$ 2PA coefficient for GaP vs $\hbar\omega$, with and without SOC. The squares are the experimental results of Furey *et al.* [13]. See text for details.

spectra show signatures that resemble the experimental results, as far as the spectral features are concerned. Indeed, the experimental results of Ref. [40], which cover a limited energy range, show a clear resonance that resembles our theoretical calculations, and the overall spectrum follows reasonably well the theoretical trend; we mention, though, that the SOC results better resemble the experimental spectrum. The magnitude of the theoretical results differs from that of the experimental results. This could be related to the fact that $\beta_{\text{eff}}(\omega)$ was measured in such a way that the crystallographic contributions of the several components of $\chi_{2\omega}^{abcd}$ were not taken into account, thus giving a 2PA that comes from the experimental "averaging" of the mixing of different Si $\chi_{2\omega}^{abcd}$ components. Indeed, as explained in Ref. [40], an "effective" $\beta_{\text{eff}}(\omega)$ was extracted by measuring the intensity $I(\omega)$ dependence of an effective absorption coefficient $\alpha_{\text{eff}}(\omega)$, whose derivative with respect to $I(\omega)$ gives the 2PA $\beta_{\text{eff}}(\omega)$, whereas, in Ref. [13], it is the 2PA $\beta_{11}^{\parallel}(\omega)$ of Eq. (47) which is measured. This could lead to the different magnitudes of 2PA measured in the two experiments; nevertheless, the spectroscopic experimental signature is similar to our 2PA $\beta_{11}^{\parallel}(\omega)$ theory.

Likewise, in Fig. 12, we show the 2PA $\beta_{11}^{\parallel}(\omega)$ for GaP. The two values of $\Sigma$ take the corresponding calculation without SOC and with SOC to the experimental 2PA gap. We see, at the onset of the two-photon transitions, a modest rise in the 2PA, followed by an almost constant 2PA and an intense and broad resonance at $\sim$1.7 eV. In this case, the first two experimental points seem to follow the monotonic increase of the theoretical result, and the third experimental point misses the strong theoretical resonance. This shows how theory could guide the experiments; had the experiment been carried out at around 1.7 eV, the resonance could have been detected.

Finally, in Appendix B, we show a comparison of the 2PA $\beta_{11}^{\parallel}(\omega)$ coefficient and Im[$\chi_{aa}(\omega)$] for GaAs, Si, and GaP (Fig. 16), and most importantly, we show $\beta_{11}^{\parallel}(\omega)$ for several semiconductors (Fig. 17), where it is worth mentioning that the 2PA energy range spans from $\sim$0.1 for InSb to $\sim$6.5 eV for diamond, and the intensity in mW$^{-1} \times 10^{-8}$ goes from $\sim$0.4 for ZnS to $\sim$70 for InSb. Our theoretical formulation leads to

results that would certainly enhance the applicability of 2PA, as it permits predictions that compare qualitatively well with available experiments.

### B. Si band structure

In Fig. 13, we show the band structure for Si including SOC, where the thick and thin lines represent degenerated states due to high-symmetry lines in the irreducible Brillouin zone (IBZ). We mention that for the energy scale used in Fig. 13, the SOC-split bands, whose energy splitting is small, are not discernible. However, in Fig. 15 of Appendix B, for GaAs, the SOC-split bands are readily seen. The arrows represent the $\hbar\omega$ photons, two of them per transition, that go from valence ($v$) to conduction bands ($c$), covering the energy range of the experimental data shown in Fig. 11, which goes from 2.05 to 2.35 eV. The $2\omega$ transitions around $\Gamma$ in the $L$-$\Gamma$-$X$ path go from $v = 2$ to degenerated $c = 2\&3$ and from degenerated $v = 3\&4$ to $c = 1$, $c = 2\&3$, and $c = 4$, where we have used "&" to denote the band degeneracy. The next sets of transitions are those away from $\Gamma$ along the $\Gamma$-$X$ path. The first set goes from $v = 3\&4$ to $c = 2$, and then there are two sets of transitions (violet-blue arrows) whose energy is $2.2 \pm .05$ eV, with the first set going from $v = 2$ to $c = 1$ and the second set going from $v = 3\&4$ to $c = 1$. Along $K$-$\Gamma$, valence bands $v = 2, 3$ and $v = 4$, as well as conduction bands $c = 1, 2$ and $c = 3$ are nondegenerated. The first set of transitions goes from $v = 4$ to $c = 1, 2, 3$, and then a second set of transitions goes from $v = 3, 4$ to $c = 1, 2, 3$. Finally, very close to $\Gamma$ and the last path, $\Gamma$-$L$ is the mirror image of $L$-$\Gamma$. A full view of the $L$-$\Gamma$-$X$-$K$-$\Gamma$-$L$ path for the bands and its $2\omega$ arrows is given in Fig. 14 of Appendix B. All these transitions contribute to the theoretical spectrum shown in Fig. 11, within $\pm 0.15$ eV of the experimental peak at 2.2 eV, and we see that most of the transitions are away from the $\Gamma$ point, as expected since the peak is away from where $\beta_{11}^{\parallel}(\omega)$ becomes finite close to the band gap of Si. It is interesting to see that the peak at 2.2 eV comes from electronic transitions that originate among different bands and in different zones of the IBZ, where those close to $X$ in the $\Gamma$-$X$ path dominate. The same analysis was
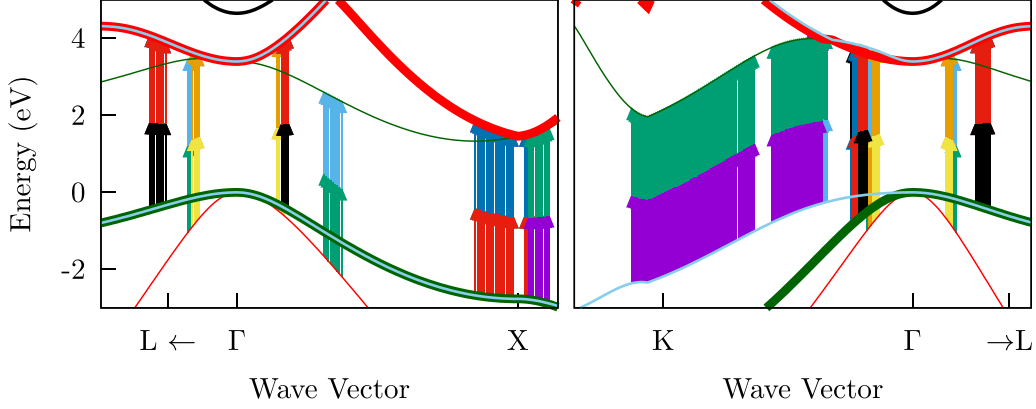
FIG. 13. Band structure of Si for $\Sigma = 1.32$ eV, where each pair of arrows denotes the corresponding $2\omega$ transitions that contribute to 2PA around $2.2 \pm 0.15$ eV, which is the peak energy of the spectrum of Fig. 11. The two $\omega$ photons that are absorbed go from a valence band (red, green, cyan) to a conduction band (blue). See text for details.

carried out for GaAs, and the band structure, along with the main results, is given in Fig. 15 of Appendix B.

## V. CONCLUSION

Within the independent-particle approach, we have presented a theoretical derivation of two-photon absorption (2PA) from semiconductors based on the length gauge formalism, where the contributions of the *intraband* $r_i$ part and the *interband* $r_e$ part of the position operator $r$ are properly accounted for and the scissors operator is included. Using time-reversal symmetry, we obtained an expression for $\chi^{abcd}(-\omega; -\omega, -\omega, \omega)$ that avoids nonphysical divergences presented in previous calculations when $\omega \to 0$ [21]. Within the independent-particle approximation, *ab initio* band structure calculations using several pseudopotential schemes that include the SOC interaction were used to calculate the 2PA coefficient, $\beta_{11}^{\parallel}(\omega)$, below the band gap of several semiconductors. In particular, $\beta_{11}^{\parallel}(\omega)$ was calculated for GaAs, Si, and GaP and compared with available experimental results. Using



FIG. 14. Band structure of Si for $\Sigma = 0.519$ eV, where each pair of arrows denotes the corresponding $2\omega$ transitions that contribute to 2PA around $2.2 \pm 0.15$ eV, which is the peak energy of the spectrum in Fig. 11. The two $\omega$ photons that are absorbed go from a valence band (red, green, cyan) to a conduction band (blue).

different values of the scissors correction, we were able to reproduce the experimental results qualitatively, showing that our calculations follow the trend of the experimental spectra signatures reported in GaAs and Si, giving a resonant behavior in the spectrum of $\beta_{11}^{\parallel}(\omega)$ for $E_g/2 < \hbar\omega < E_g$. The spectrum reported for GaAs mainly comes from the last valence band to the first conduction band around the $\Gamma$ point of the IBZ; in contrast, for Si there are transitions from the second, third, and fourth valence bands to the second, third, fourth, and fifth conduction bands, which are spread over the IBZ, in particular, along the $\Gamma$-$X$ path, thus explaining the complexity of the 2PA spectrum for this material. Moreover, the $2\omega$ and $1\omega$ terms of $\chi^{abcd}(-\omega; -\omega, -\omega, \omega)$ are analyzed to obtain a complete third-order optical response. The position matrix elements are distinguished in the *intraband* $r_i$ part and the *interband* $r_e$ part, allowing us to disregard numerically negligible terms in $\chi^{abcd}(-\omega; -\omega, -\omega, \omega)$ that come from three- and four-band transitions. To strengthen our results, a full *GW* calculation, which goes beyond the scissors approximation, would be able to produce a band structure that, through our expression for $\chi^{abcd}(-\omega; -\omega, -\omega, \omega)$, could match the experiment on firmer grounds; however, the large number of $k$ points needed to achieve convergence ($\sim$60 000) represents a numerical challenge in its own terms. Moreover, it would be desirable to go beyond the independent-particle approximation and develop the 2PA theory including the electron-hole interaction. However, including the electron-hole interaction even for the linear response is a very demanding problem, not only with regard to the theoretical part, but also with regard to the numerical computation, as described in Refs. [26,42]; this would constitute a very challenging problem that ought to be pursued in the future. Nonetheless, our results show the
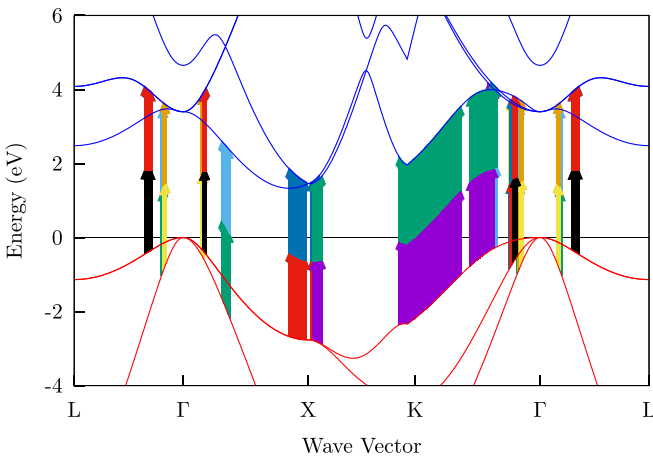
TABLE I. Relations obtained from time-reversal symmetry [43].

$$\omega_{nm}(-\boldsymbol{k}) = \omega_{nm}(\boldsymbol{k}),$$
$$r_{nm}^{a}(-\boldsymbol{k}) = r_{mn}^{a}(\boldsymbol{k})$$
$$r_{nm}^{a}(-\boldsymbol{k})_{;k^b} = -r_{mn}^{a}(\boldsymbol{k})_{;k^b}$$
$$v_{mn}^{a}(-\boldsymbol{k}) = -v_{nm}^{a}(\boldsymbol{k})$$
$$v_{mn}^{a}(-\boldsymbol{k})_{;k^b} = v_{nm}^{a}(\boldsymbol{k})_{;k^b}$$
$$\Delta_{nm}^{a}(-\boldsymbol{k}) = -\Delta_{nm}^{a}(\boldsymbol{k})$$

correct order of magnitude and spectral features with which an adequate semiconductor could be chosen for myriad of applications of 2PA. Thus our predictions of 2PA that cover both a wide spectral range and a wide intensity range for the semiconductors which are commonly used in semiconductor technology will certainly motivate 2PA experimental investigation for these materials.

## APPENDIX A: DERIVATION OF $\chi^{\mathrm{abcd}}(-\omega; -\omega, -\omega, \omega)$

In this Appendix, we give the main steps to obtain the 2PA $\chi^{\mathrm{abcd}}(-\omega; -\omega, -\omega, \omega)$ susceptibility of Eq. (40). Using Eq. (36) and the chain rule,

$$\varrho_{nm;k^{\mathrm{d}}}^{(2)}(-2\omega, \boldsymbol{k}) = \frac{e^2}{\hbar^2}\left(\frac{\mathcal{G}_{nm;k^{\mathrm{d}}}^{\mathrm{bc}}(-\omega, \boldsymbol{k})}{\omega_{nm}(\boldsymbol{k}) - 2\tilde{\omega}} + \mathcal{G}_{nm}^{\mathrm{bc}}(-\omega, \boldsymbol{k})\left(\frac{1}{\omega_{nm}(\boldsymbol{k}) - 2\tilde{\omega}}\right)_{;k^{\mathrm{d}}}\right), \tag{A1}$$

which from Eq. (40) leads to

$$\chi^{\mathrm{abcd}}(-\omega; -\omega, -\omega, \omega) = \frac{ie^4}{\hbar^3\tilde{\omega}}\int\frac{d\boldsymbol{k}}{8\pi^3}\sum_{m\neq n\neq\ell}\left(\frac{v_{mn}^{\mathrm{a}}(\boldsymbol{k})r_{n\ell}^{\mathrm{d}}(\boldsymbol{k})\mathcal{G}_{\ell m}^{\mathrm{bc}}(-\omega, \boldsymbol{k})}{\omega_{\ell m}(\boldsymbol{k}) - 2\tilde{\omega}} - \frac{v_{mn}^{\mathrm{a}}(\boldsymbol{k})\mathcal{G}_{n\ell}^{\mathrm{bc}}(-\omega, \boldsymbol{k})r_{\ell m}^{\mathrm{d}}(\boldsymbol{k})}{\omega_{n\ell}(\boldsymbol{k}) - 2\tilde{\omega}}\right.$$
$$\left. + i\frac{v_{mn}^{\mathrm{a}}(\boldsymbol{k})\mathcal{G}_{nm;k^{\mathrm{d}}}^{\mathrm{bc}}(-\omega, \boldsymbol{k})}{\omega_{nm}(\boldsymbol{k}) - 2\tilde{\omega}} + iv_{mn}^{\mathrm{a}}(\boldsymbol{k})\mathcal{G}_{nm}^{\mathrm{bc}}(-\omega, \boldsymbol{k})\left(\frac{1}{\omega_{nm}(\boldsymbol{k}) - 2\tilde{\omega}}\right)_{;k^d}\right)\frac{1}{\omega_{nm}(\boldsymbol{k}) - \tilde{\omega}}. \tag{A2}$$

Integrating by parts the last term of the above equation, we obtain that

$$\chi^{\mathrm{abcd}}(-\omega; -\omega, -\omega, \omega) = \frac{ie^4}{\hbar^3\tilde{\omega}}\int\frac{d\boldsymbol{k}}{8\pi^3}\sum_{m\neq n}\left[\left(-i\frac{v_{mn;k^{\mathrm{d}}}^{\mathrm{a}}(\boldsymbol{k})\mathcal{G}_{nm}^{\mathrm{bc}}(-\omega, \boldsymbol{k})}{(\omega_{nm}(\boldsymbol{k}) - 2\tilde{\omega})(\omega_{nm}(\boldsymbol{k}) - \tilde{\omega})}\|_1 + i\frac{v_{mn}^{\mathrm{a}}(\boldsymbol{k})\Delta_{nm}^{\mathrm{d}}(\boldsymbol{k})\mathcal{G}_{nm}^{\mathrm{bc}}(-\omega, \boldsymbol{k})}{(\omega_{nm}(\boldsymbol{k}) - 2\tilde{\omega})(\omega_{nm}(\boldsymbol{k}) - \tilde{\omega})^2}\|_2\right)\right.$$
$$\left. + \sum_{\ell\neq m,n}\left(-\frac{v_{mn}^{\mathrm{a}}(\boldsymbol{k})r_{n\ell}^{\mathrm{d}}(\boldsymbol{k})\mathcal{G}_{\ell m}^{\mathrm{bc}}(-\omega, \boldsymbol{k})}{(\omega_{\ell m}(\boldsymbol{k}) - 2\tilde{\omega})(\omega_{nm}(\boldsymbol{k}) - \tilde{\omega})}\|_3 + \frac{v_{mn}^{\mathrm{a}}(\boldsymbol{k})r_{\ell m}^{\mathrm{d}}(\boldsymbol{k})\mathcal{G}_{n\ell}^{\mathrm{bc}}(-\omega, \boldsymbol{k})}{(\omega_{n\ell}(\boldsymbol{k}) - 2\tilde{\omega})(\omega_{nm}(\boldsymbol{k}) - \tilde{\omega})}\|_4\right)\right], \tag{A3}$$

where we have labeled the four terms from 1 to 4 and used the fact that [27]

$$\omega_{m;k^{\mathrm{a}}}(\boldsymbol{k}) = v_{mm}^{\mathrm{a}}(\boldsymbol{k}) \tag{A4}$$

is the velocity of band $m$, and we defined

$$\Delta_{mn}^{\mathrm{a}}(\boldsymbol{k}) \equiv v_{mm}^{\mathrm{a}}(\boldsymbol{k}) - v_{nn}^{\mathrm{a}}(\boldsymbol{k}). \tag{A5}$$

From Eq. (19),

$$v_{nm;k^{\mathrm{b}}}^{\mathrm{a}} = i\Delta_{nm}^{\mathrm{b}}r_{nm}^{\mathrm{a}} + i\omega_{nm}r_{nm;k^{\mathrm{b}}}^{\mathrm{a}}, \tag{A6}$$

where [18,31]

$$r_{nm;k^{\mathrm{a}}}^{\mathrm{b}} = \frac{r_{nm}^{\mathrm{a}}\Delta_{mn}^{\mathrm{b}} + r_{nm}^{\mathrm{b}}\Delta_{mn}^{\mathrm{a}}}{\omega_{nm}} + \frac{i}{\omega_{nm}}\sum_{\ell\neq m,n}\left(\omega_{\ell m}r_{n\ell}^{\mathrm{a}}r_{\ell m}^{\mathrm{b}} - \omega_{n\ell}r_{n\ell}^{\mathrm{b}}r_{\ell m}^{\mathrm{a}}\right). \tag{A7}$$

Apparently, Eq. (A3) diverges as $\omega$ goes to zero; however, in what follows, this divergence will be shown to cancel out by invoking time-reversal symmetry (TRS) [43]. To show the mathematical steps involved in reducing Eq. (A3) into a $1/\omega$-divergent-less expression, we take as an example its second term, $\chi_2^{\mathrm{abcd}}$ (omitting the $\omega$ arguments), and write

$$\chi_2^{\mathrm{abcd}} = -\frac{e^4}{\hbar^3\tilde{\omega}}\int\frac{d\boldsymbol{k}}{8\pi^3}\sum_{m\neq n}\frac{v_{mn}^{\mathrm{a}}(\boldsymbol{k})\Delta_{nm}^{\mathrm{d}}(\boldsymbol{k})\mathcal{G}_{nm}^{\mathrm{bc}}(-\omega, \boldsymbol{k})}{(\omega_{nm}(\boldsymbol{k}) - 2\tilde{\omega})(\omega_{nm}(\boldsymbol{k}) - \tilde{\omega})^2}, \tag{A8}$$

where from Eqs. (27) and (37), we obtain that

$$\mathcal{G}_{nm}^{\mathrm{bc}} = \frac{if_{mn}r_{nm;k^{\mathrm{b}}}^{\mathrm{c}}}{\omega_{nm} - \tilde{\omega}} - \frac{if_{mn}r_{nm}^{\mathrm{c}}\Delta_{nm}^{\mathrm{b}}}{(\omega_{nm} - \tilde{\omega})^2} + \sum_{\ell\neq mn}\left(\frac{f_{m\ell}r_{\ell m}^{\mathrm{c}}r_{n\ell}^{\mathrm{b}}}{\omega_{\ell m} - \tilde{\omega}} - \frac{f_{\ell n}r_{n\ell}^{\mathrm{c}}r_{\ell m}^{\mathrm{b}}}{\omega_{n\ell} - \tilde{\omega}}\right), \tag{A9}$$

where we omitted the $(-\omega, \boldsymbol{k})$ and $(\boldsymbol{k})$ arguments to save space. After substituting Eq. (A9) into (A8), we split the result into three terms and perform a partial fraction expansion on $\omega$, for each of the three terms. For the first term, we obtain that

$$\chi_{2,1}^{\text{abcd}} \propto \frac{1}{\tilde{\omega}(\omega_{nm} - 2\tilde{\omega})(\omega_{nm} - \tilde{\omega})^3} \equiv \tilde{W}_{nm}^{(2,1)} = \frac{1}{\omega_{nm}^4 \tilde{\omega}} + W_{nm,\omega}^{(2,1)} + W_{nm,2\omega}^{(2,1)}, \tag{A10}$$

where

$$W_{nm,\omega}^{(2,1)} = -\frac{7}{\omega_{nm}^4(\omega_{nm} - \tilde{\omega})} - \frac{3}{\omega_{nm}^3(\omega_{nm} - \tilde{\omega})^2} - \frac{1}{\omega_{nm}^2(\omega_{nm} - \tilde{\omega})^3} \tag{A11}$$

and

$$W_{nm,2\omega}^{(2,1)} = \frac{16}{\omega_{nm}^4(\omega_{nm} - 2\tilde{\omega})}. \tag{A12}$$

In Eq. (A10), the $1/\tilde{\omega}$ divergent term is isolated from the rest of the nondivergent $\tilde{\omega}$ and $2\tilde{\omega}$ terms given in $W_{nm,\omega}^{(2,1)}$ and $W_{nm,2\omega}^{(2,1)}$, respectively. Using the TRS relations shown in Table I, we obtain that

$$\chi_{2,1}^{\text{abcd}} = -i\frac{e^4}{\hbar^3} \int_{k>0} \frac{d\boldsymbol{k}}{8\pi^3} \sum_{m \neq n} f_{mn}(\boldsymbol{k}) \tilde{W}_{nm}^{(4,1)}(\boldsymbol{k}) \left( r_{nm;k^b}^c(\boldsymbol{k}) v_{mn}^a(\boldsymbol{k}) \Delta_{nm}^d(\boldsymbol{k}) + r_{nm;k^b}^c(-\boldsymbol{k}) v_{mn}^a(-\boldsymbol{k}) \Delta_{nm}^d(-\boldsymbol{k}) \right)$$

$$= \frac{e^4}{\hbar^3} \int \frac{d\boldsymbol{k}}{8\pi^3} \sum_{m \neq n} f_{mn}(\boldsymbol{k}) \tilde{W}_{nm}^{(4,1)}(\boldsymbol{k}) \Delta_{nm}^d(\boldsymbol{k}) \text{Im}[r_{nm;k^b}^c(\boldsymbol{k}) v_{mn}^a(\boldsymbol{k})], \tag{A13}$$

and using $\sum_{mn} \mathcal{F}_{mn} = \sum_{m<n}(\mathcal{F}_{mn} + \mathcal{F}_{nm})$, the above equation is converted into

$$\chi_{2,1}^{\text{abcd}} = \frac{e^4}{\hbar^3} \int \frac{d\boldsymbol{k}}{8\pi^3} \sum_{m<n} f_{mn}(\boldsymbol{k}) \Delta_{nm}^d(\boldsymbol{k}) \text{Im}[r_{nm;k^b}^c(\boldsymbol{k}) v_{mn}^a(\boldsymbol{k})] \left( \tilde{W}_{nm}^{(2,1)}(\boldsymbol{k}) - \tilde{W}_{mn}^{(2,1)}(\boldsymbol{k}) \right), \tag{A14}$$

where we used the fact that $\mathcal{O}_{nm} = \mathcal{O}_{mn}^*$, with $\hat{O}$ being a Hermitian operator, and that $\text{Im}[z^*] = -\text{Im}[z]$. From Eq. (A10),

$$\tilde{W}_{nm}^{(2,1)} - \tilde{W}_{mn}^{(2,1)} = W_{nm,\omega}^{(2,1)} + W_{nm,2\omega}^{(2,1)} + \frac{1}{\omega_{nm}^4 \omega} - W_{mn,\omega}^{(2,1)} - W_{mn,2\omega}^{(2,1)} - \frac{1}{\omega_{mn}^4 \omega}$$

$$= W_{nm,\omega}^{(2,1)} + W_{nm,2\omega}^{(2,1)} - W_{mn,\omega}^{(2,1)} - W_{mn,2\omega}^{(2,1)}, \tag{A15}$$

since $\omega_{nm}^4 = \omega_{mn}^4$, and therefore the divergent $1/\omega$ cancels out due to TRS. Thus

$$\chi_{2,1}^{\text{abcd}} = \frac{e^4}{\hbar^3} \int \frac{d\boldsymbol{k}}{8\pi^3} \sum_{vc} \Delta_{cv}^d(\boldsymbol{k}) \text{Im}[r_{cv;k^b}^c(\boldsymbol{k}) v_{vc}^a(\boldsymbol{k})] \left( W_{cv,\omega}^{(2,1)}(\boldsymbol{k}) - W_{vc,\omega}^{(2,1)}(\boldsymbol{k}) + W_{cv,2\omega}^{(2,1)}(\boldsymbol{k}) - W_{vc,2\omega}^{(2,1)}(\boldsymbol{k}) \right), \tag{A16}$$

since $m < n$ implies from $f_{mn}(\boldsymbol{k})$ that $m = v$ and $n = c$, with $v$ and $c$ being valence and conduction states, respectively. We see that $\chi_{2,1}^{\text{abcd}}$ could be split into $1\omega$ and $2\omega$ terms, as follows:

$$\chi_{2,1,p\omega}^{\text{abcd}} = \frac{e^4}{\hbar^3} \int \frac{d\boldsymbol{k}}{8\pi^3} \sum_{vc} \Delta_{cv}^d(\boldsymbol{k}) \text{Im}[r_{cv;k^b}^c(\boldsymbol{k}) v_{vc}^a(\boldsymbol{k})] \left( W_{cv,p\omega}^{(2,1)}(\boldsymbol{k}) - W_{vc,p\omega}^{(2,1)}(\boldsymbol{k}) \right), \tag{A17}$$

where $p = 1, 2$ and $\chi_{2,1}^{\text{abcd}} = \chi_{2,1,\omega}^{\text{abcd}} + \chi_{2,1,2\omega}^{\text{abcd}}$.

Since we are mainly interested in 2PA for photon energies below the gap, we focus on the $2\omega$ term. Then, taking $\eta \to 0$ upon $W_{vc,2\omega}^{(2,1)}(\boldsymbol{k})$ leads to a nonresonant denominator, and from $W_{cv,2\omega}^{(2,1)}(\boldsymbol{k})$, we obtain

$$\text{Im}\left[\chi_{2,1,2\omega}^{\text{abcd}}\right] = \frac{\pi e^4}{\hbar^3} \int \frac{d\boldsymbol{k}}{8\pi^3} \sum_{vc} \frac{16\Delta_{cv}^d(\boldsymbol{k}) \text{Im}\left[r_{cv;k^b}^c(\boldsymbol{k}) v_{vc}^a(\boldsymbol{k})\right]}{\omega_{cv}^4(\boldsymbol{k})} \delta(\omega_{cv}(\boldsymbol{k}) - 2\omega), \tag{A18}$$

which is a closed expression that can be readily evaluated, and through its Kramers-Kronig transformation, the real part of $\chi_{2,1,2\omega}^{\text{abcd}}$ could be calculated.

Using the above procedure, we obtain that

$$\chi_{2,2,p\omega}^{\text{abcd}} = -\frac{e^4}{\hbar^3} \int \frac{d\boldsymbol{k}}{8\pi^3} \sum_{vc} \Delta_{cv}^b(\boldsymbol{k}) \Delta_{cv}^d(\boldsymbol{k}) \text{Im}\left[v_{vc}^a(\boldsymbol{k}) r_{cv}^c(\boldsymbol{k})\right] \left( W_{cv,p\omega}^{(2,2)}(\boldsymbol{k}) + W_{vc,p\omega}^{(2,2)}(\boldsymbol{k}) \right), \tag{A19}$$

with

$$W_{nm,\omega}^{(2,2)} = -\frac{15}{\omega_{nm}^5(\omega_{nm} - \omega)} - \frac{7}{\omega_{nm}^4(\omega_{nm} - \omega)^2} - \frac{3}{\omega_{nm}^3(\omega_{nm} - \omega)^3} - \frac{1}{\omega_{nm}^2(\omega_{nm} - \omega)^4} \tag{A20}$$

and

$$W_{nm,2\omega}^{(2,2)} = \frac{32}{\omega_{nm}^5(\omega_{nm} - 2\omega)}. \tag{A21}$$

The $2\omega$ term is given by

$$\mathrm{Im}\big[\chi_{2,2,2\omega}^{abcd}\big] = -\frac{\pi e^4}{\hbar^3} \int \frac{d\boldsymbol{k}}{8\pi^3} \sum_{vc} \frac{32\Delta_{cv}^b(\boldsymbol{k})\Delta_{cv}^d(\boldsymbol{k})\mathrm{Im}\big[v_{vc}^a(\boldsymbol{k})r_{cv}^c(\boldsymbol{k})\big]}{\omega_{cv}^5(\boldsymbol{k})}\delta(\omega_{cv}(\boldsymbol{k}) - 2\omega). \tag{A22}$$

Lastly,

$$\chi_{2,3,p\omega}^{abcd} = -\frac{e^4}{\hbar^3} \int \frac{d\boldsymbol{k}}{8\pi^3} \sum_{m \neq n \neq \ell} f_{m\ell}(\boldsymbol{k})\Delta_{nm}^d(\boldsymbol{k})\mathrm{Re}\big[r_{\ell m}^c(\boldsymbol{k})r_{n\ell}^b(\boldsymbol{k})v_{mn}^a(\boldsymbol{k})\big]\big(W_{nm\ell,p\omega}^{(2,3,1)}(\boldsymbol{k}) - W_{mn\ell,p\omega}^{(2,3,2)}(\boldsymbol{k})\big), \tag{A23}$$

where

$$W_{nm\ell,\omega}^{(2,3,1)} = -\frac{3\omega_{\ell m} - 4\omega_{nm}}{\omega_{nm}^3(\omega_{nm} - \omega_{\ell m})^2(\omega_{nm} - \tilde{\omega})} + \frac{1}{\omega_{nm}^2(\omega_{nm} - \omega_{\ell m})(\omega_{nm} - \tilde{\omega})^2}$$
$$- \frac{1}{\omega_{\ell m}(\omega_{\ell m} - \omega_{nm})^2(2\omega_{\ell m} - \omega_{nm})(\omega_{\ell m} - \tilde{\omega})}, \tag{A24}$$

$$W_{nm\ell,2\omega}^{(2,3,1)} = -\frac{16}{\omega_{nm}^3(\omega_{nm} - 2\omega_{\ell m})(\omega_{nm} - 2\tilde{\omega})}, \tag{A25}$$

$$W_{nm\ell,\omega}^{(2,3,2)} = -\frac{3\omega_{n\ell} - 4\omega_{nm}}{\omega_{nm}^3(\omega_{nm} - \omega_{n\ell})^2(\omega_{nm} - \tilde{\omega})} + \frac{1}{\omega_{nm}^2(\omega_{nm} - \omega_{n\ell})(\omega_{nm} - \tilde{\omega})^2}$$
$$- \frac{1}{\omega_{n\ell}(\omega_{n\ell} - \omega_{nm})^2(2\omega_{n\ell} - \omega_{nm})(\omega_{n\ell} - \tilde{\omega})}, \tag{A26}$$

and

$$W_{nm\ell,2\omega}^{(2,3,2)} = -\frac{16}{\omega_{nm}^3(\omega_{nm} - 2\omega_{n\ell})(\omega_{nm} - 2\tilde{\omega})}. \tag{A27}$$

Then,

$$\chi_2^{abcd} = \sum_{p=1}^2 \big(\chi_{2,1,p\omega}^{abcd} + \chi_{2,2,p\omega}^{abcd} + \chi_{2,3,p\omega}^{abcd}\big). \tag{A28}$$

Following the same steps that lead to $\chi_2^{abcd}$, we obtain that

$$\chi_1^{abcd} = \sum_{p=1}^2 \big(\chi_{1,1,p\omega}^{abcd} + \chi_{1,2,p\omega}^{abcd} + \chi_{1,3,p\omega}^{abcd}\big), \tag{A29}$$

where, for $\chi_{1,1,p\omega}^{abcd}$, we obtain

$$\chi_{1,1,p\omega}^{abcd} = -\frac{e^4}{\hbar^3} \int \frac{d\boldsymbol{k}}{8\pi^3} \sum_{m \neq n} f_{mn}\mathrm{Im}\big[v_{mn;k^d}^a(\boldsymbol{k})r_{nm;k^b}^c(\boldsymbol{k})\big]W_{nm,p\omega}^{(1,1)}, \tag{A30}$$

with

$$W_{nm,\omega}^{(1,1)} = \frac{-3}{\omega_{nm}^3(\omega_{nm} - \tilde{\omega})} - \frac{1}{\omega_{nm}^2(\omega_{nm} - \tilde{\omega})^2},$$
$$W_{nm2,\omega}^{(1,1)} = \frac{8}{\omega_{nm}^3(\omega_{nm} - 2\tilde{\omega})}, \tag{A31}$$

and

$$\chi_{1,1,2\omega}^{abcd} = -\frac{e^4}{\hbar^3} \int \frac{d\boldsymbol{k}}{8\pi^3} \sum_{vc} \frac{8\mathrm{Im}\big[v_{vc;k^d}^a(\boldsymbol{k})r_{cv;k^b}^c(\boldsymbol{k})\big]}{\omega_{cv}^3(\boldsymbol{k})}\delta(\omega_{cv}(\boldsymbol{k}) - 2\tilde{\omega}). \tag{A32}$$

$\chi_{1,2,p\omega}^{abcd}$ is given by

$$\chi_{1,2,p\omega}^{abcd} = \frac{e^4}{\hbar^3} \int \frac{d\boldsymbol{k}}{8\pi^3} \sum_{m \neq n} f_{mn}\Delta_{nm}^b\mathrm{Im}\big[r_{nm}^c v_{mn;k^d}^a\big]W_{nm,p\omega}^{(1,2)}, \tag{A33}$$

with

$$W_{nm,\omega}^{(1,2)} = \frac{-7}{\omega_{nm}^4(\omega_{nm} - \tilde{\omega})} - \frac{3}{\omega_{nm}^3(\omega_{nm} - \tilde{\omega})^2} - \frac{1}{\omega_{nm}^2(\omega_{nm} - \tilde{\omega})^3},$$

$$W_{nm,2\omega}^{(1,2)} = \frac{16}{\omega_{nm}^4(\omega_{nm} - 2\omega)}, \tag{A34}$$

and

$$\chi_{1,2,2\omega}^{abcd} = \frac{e^4}{\hbar^3} \int \frac{d\boldsymbol{k}}{8\pi^3} \sum_{vc} \frac{16\Delta_{cv}^b(\boldsymbol{k})\mathrm{Im}\big[r_{cv}^c(\boldsymbol{k})v_{vc;k^d}^a(\boldsymbol{k})\big]}{\omega_{cv}^4(\boldsymbol{k})} \delta(\omega_{cv}(\boldsymbol{k}) - 2\omega). \tag{A35}$$

$\chi_{1,3,p\omega}^{abcd}$ is given by

$$\chi_{1,3,p\omega}^{abcd} = \frac{e^4}{\hbar^3} \int \frac{d\boldsymbol{k}}{8\pi^3} \sum_{m \neq n \neq \ell} f_{m\ell}\mathrm{Re}\big[v_{mn;k^d}^a r_{\ell m}^c r_{n\ell}^b\big]\big(W_{nm\ell,p\omega}^{(1,3,1)} - W_{mn\ell,p\omega}^{(1,3,2)}\big), \tag{A36}$$

where

$$W_{nm\ell,\omega}^{(1,3,1)} = \frac{1}{\omega_{nm}^2\omega_{n\ell}(\omega_{nm} - \tilde{\omega})} - \frac{1}{\omega_{\ell m}\omega_{\ell n}(\omega_{nm} - 2\omega_{\ell m})(\omega_{\ell m} - \tilde{\omega})},$$

$$W_{nm\ell,2\omega}^{(1,3,1)} = -\frac{8}{\omega_{nm}^2(\omega_{nm} - 2\omega_{\ell m})(\omega_{nm} - 2\tilde{\omega})},$$

$$W_{nm\ell,\omega}^{(1,3,2)} = \frac{1}{\omega_{nm}^2\omega_{\ell m}(\omega_{nm} - \tilde{\omega})} + \frac{1}{\omega_{n\ell}\omega_{m\ell}(2\omega_{n\ell} - \omega_{nm})(\omega_{n\ell} - \tilde{\omega})},$$

$$W_{nm\ell,2\omega}^{(1,3,2)} = -\frac{8}{\omega_{nm}^2(\omega_{nm} - 2\omega_{n\ell})(\omega_{nm} - 2\tilde{\omega})}. \tag{A37}$$

For $\chi_3^{abcd}$ and $\chi_4^{abcd}$, we write

$$\chi_3^{abcd} + \chi_4^{abcd} = \sum_{p=1}^2 \Big(\big(\chi_{3,1,p\omega}^{abcd} + \chi_{4,1,p\omega}^{abcd}\big) + \big(\chi_{3,2,p\omega}^{abcd} + \chi_{4,2,p\omega}^{abcd}\big) + \big(\chi_{3,3,2,p\omega}^{abcd} + \chi_{4,3,1,p\omega}^{abcd}\big) + \big(\chi_{3,3,1,p\omega}^{abcd} + \chi_{4,3,2,p\omega}^{abcd}\big)\Big), \tag{A38}$$

where we have grouped the $\chi$'s that have common factors within the small parentheses. We have that

$$\chi_{3,1,p\omega}^{abcd} + \chi_{4,1,p\omega}^{abcd} = -\frac{e^4}{\hbar^3} \int \frac{d\boldsymbol{k}}{8\pi^3} \sum_{m \neq n \neq l} f_{nl}\mathrm{Re}\big[v_{nm}^a r_{ml}^d r_{ln;k^b}^c\big]\big(W_{nml,p\omega}^{(4,1)} - W_{nml,p\omega}^{(3,1)}\big), \tag{A39}$$

where

$$W_{nml,\omega}^{(3,1)} = \frac{1}{\omega_{nl}^2\omega_{ml}(\omega_{nl} - \tilde{\omega})} + \frac{1}{\omega_{nm}\omega_{lm}(2\omega_{nm} - \omega_{nl})(\omega_{nm} - \tilde{\omega})},$$

$$W_{nml,2\omega}^{(3,1)} = -\frac{8}{\omega_{nl}^2(\omega_{nl} - 2\omega_{nm})(\omega_{nl} - 2\tilde{\omega})},$$

$$W_{nml,\omega}^{(4,1)} = \frac{1}{\omega_{ln}^2\omega_{lm}(\omega_{ln} - \tilde{\omega})} + \frac{1}{\omega_{mn}\omega_{ml}(2\omega_{mn} - \omega_{ln})(\omega_{mn} - \tilde{\omega})},$$

$$W_{nml,2\omega}^{(4,1)} = -\frac{8}{\omega_{ln}^2(\omega_{ln} - 2\omega_{mn})(\omega_{ln} - 2\tilde{\omega})}. \tag{A40}$$

Now,

$$\chi_{3,2,p\omega}^{abcd} + \chi_{4,2,p\omega}^{abcd} = \frac{e^4}{\hbar^3} \int \frac{d\boldsymbol{k}}{8\pi^3} \sum_{m \neq n \neq l} f_{nl}\Delta_{ln}^b\mathrm{Re}\big[v_{nm}^a r_{ml}^d r_{ln}^c\big]\big(W_{nml,p\omega}^{(4,2)} - W_{nml,p\omega}^{(3,2)}\big), \tag{A41}$$

with

$$W_{nml,\omega}^{(3,2)} = -\frac{3\omega_{nm} - 4\omega_{nl}}{\omega_{nl}^3(\omega_{nl} - \omega_{nm})^2(\omega_{nl} - \tilde{\omega})} + \frac{1}{\omega_{nl}^2(\omega_{nl} - \omega_{nm})(\omega_{nl} - \tilde{\omega})^2} - \frac{1}{\omega_{nm}(\omega_{nm} - \omega_{nl})^2(2\omega_{nm} - \omega_{nl})(\omega_{nm} - \tilde{\omega})},$$

$$W_{nml,2\omega}^{(3,2)} = -\frac{16}{\omega_{nl}^3(\omega_{nl} - 2\omega_{nm})(\omega_{nl} - 2\tilde{\omega})},$$

$$W_{nml,\omega}^{(4,2)} = -\frac{3\omega_{mn} - 4\omega_{ln}}{\omega_{ln}^3 (\omega_{ln} - \omega_{mn})^2 (\omega_{ln} - \tilde{\omega})} + \frac{1}{\omega_{ln}^2 (\omega_{ln} - \omega_{mn})(\omega_{ln} - \tilde{\omega})^2} - \frac{1}{\omega_{mn}(\omega_{mn} - \omega_{ln})^2 (2\omega_{mn} - \omega_{ln})(\omega_{mn} - \tilde{\omega})},$$

$$W_{nml,2\omega}^{(4,2)} = -\frac{16}{\omega_{ln}^3 (\omega_{ln} - 2\omega_{mn})(\omega_{ln} - 2\tilde{\omega})}. \tag{A42}$$

Next,

$$\chi_{3,3,1,p\omega}^{\text{abcd}} = \chi_{4,3,2,p\omega}^{\text{abcd}} = \frac{e^4}{\hbar^3} \int \frac{d\boldsymbol{k}}{8\pi^3} \sum_{m \neq n \neq l \neq q} f_{ql} \text{Im}\big[v_{nm}^{\text{a}} r_{ml}^{\text{d}} r_{lq}^{\text{c}} r_{qn}^{\text{b}}\big] \big(W_{nmlq,p\omega}^{(4,3,2)} + W_{nmlq,p\omega}^{(3,3,1)}\big), \tag{A43}$$

where

$$W_{nmlq,\omega}^{(3,3,1)} = \frac{1}{\omega_{nm}(2\omega_{nm} - \omega_{nl})(\omega_{nm} - \omega_{ql})(\omega_{nm} - \tilde{\omega})} + \frac{1}{\omega_{ql}(2\omega_{ql} - \omega_{nl})(\omega_{ql} - \omega_{nm})(\omega_{ql} - \tilde{\omega})},$$

$$W_{nmlq,2\omega}^{(3,3,1)} = \frac{8}{\omega_{nl}(\omega_{nl} - 2\omega_{nm})(\omega_{nl} - 2\omega_{ql})(\omega_{nl} - 2\tilde{\omega})},$$

$$W_{nmlq,\omega}^{(4,3,2)} = \frac{1}{\omega_{mn}(2\omega_{mn} - \omega_{ln})(\omega_{mn} - \omega_{lq})(\omega_{mn} - \tilde{\omega})} + \frac{1}{\omega_{lq}(2\omega_{lq} - \omega_{ln})(\omega_{lq} - \omega_{mn})(\omega_{lq} - \tilde{\omega})},$$

$$W_{nmlq,2\omega}^{(4,3,2)} = \frac{8}{\omega_{ln}(\omega_{ln} - 2\omega_{mn})(\omega_{ln} - 2\omega_{lq})(\omega_{ln} - 2\tilde{\omega})}. \tag{A44}$$

Finally,

$$\chi_{3,3,2,p\omega}^{\text{abcd}} + \chi_{4,3,1,p\omega}^{\text{abcd}} = -\frac{e^4}{\hbar^3} \sum_{m \neq n \neq l \neq q\boldsymbol{k}} f_{nq} \text{Im}\big[v_{nm}^{\text{a}} r_{ml}^{\text{d}} r_{qn}^{\text{c}} r_{lq}^{\text{b}}\big] \Big(W_{nmlq,p\omega}^{(4,3,1)} + W_{nmlq,p\omega}^{(3,3,2)}\Big), \tag{A45}$$

where

$$W_{nmlq,\omega}^{(3,3,2)} = \frac{1}{\omega_{nm}\omega_{qm}(2\omega_{nm} - \omega_{nl})(\omega_{nm} - \tilde{\omega})} + \frac{1}{\omega_{nq}\omega_{mq}(2\omega_{nq} - \omega_{nl})(\omega_{nq} - \tilde{\omega})},$$

$$W_{nmlq,2\omega}^{(3,3,2)} = \frac{8}{\omega_{nl}(\omega_{nl} - 2\omega_{nm})(\omega_{nl} - 2\omega_{nq})(\omega_{nl} - 2\tilde{\omega})},$$

$$W_{nmlq,\omega}^{(4,3,1)} = \frac{1}{\omega_{mn}\omega_{mq}(2\omega_{mn} - \omega_{ln})(\omega_{mn} - \tilde{\omega})} + \frac{1}{\omega_{qn}\omega_{qm}(2\omega_{qn} - \omega_{ln})(\omega_{qn} - \tilde{\omega})},$$

$$W_{nmlq,2\omega}^{(4,3,1)} = \frac{8}{\omega_{ln}(\omega_{ln} - 2\omega_{mn})(\omega_{ln} - 2\omega_{qn})(\omega_{ln} - 2\tilde{\omega})}. \tag{A46}$$

TABLE II. Room-temperature experimental lattice constant $a_0$ in bohrs along with the experimental and theoretical direct-band-gap energies $E_g$ in eV of the semiconductors studied in this paper without SOC. For the indirect semiconductors, we only report the direct gap. We mention that for InSb, InAs, and Ge the notation "≈0" means that the theoretical gaps are of the order of $\approx 10^{-11}$ eV.

| | $a_0$ | Expt. | LDA-HGH | GGA-HGH | $E_g$ GGA-PSPNC | LDA-PSPNC | mGGA-HGH |
|---|---|---|---|---|---|---|---|
| | | | | Direct semiconductors without SOC | | | |
| GaAs | 10.684 | 1.424 | 0.470 | 0.509 | 0.572 | 0.597 | 1.235 |
| InSb | 12.243 | 0.18 | ≈0 | ≈0 | 0.053 | 0.098 | 0.305 |
| GaSb | 11.519 | 0.75 | 0.099 | 0.113 | 0.203 | 0.260 | 0.613 |
| InAs | 11.448 | 0.345 | ≈0 | ≈0 | 0.113 | 0.128 | 0.522 |
| ZnS | 10.223 | 3.54 | 2.642 | 2.818 | 2.033 | 1.698 | 3.898 |
| ZnSe | 10.711 | 2.82 | 1.670 | 1.830 | 1.253 | 0.967 | 2.728 |
| CdTe | 12.24 | 1.5 | 1.029 | 1.168 | 0.7203 | 0.458 | 1.772 |
| | | | | Indirect semiconductors without SOC | | | |
| Si | 10.26 | 3.4 | 2.555 | 2.610 | 2.570 | 2.516 | 2.880 |
| GaP | 10.3 | 2.78 | 1.795 | 1.849 | 1.978 | 1.960 | 2.723 |
| Diamond | 6.74 | 6.5 | 5.677 | 5.743 | 5.664 | 5.593 | 5.865 |
| Ge | 10.69 | 0.805 | ≈0 | ≈0 | 0.007 | 0.091 | 0.516 |
| BeTe | 10.61 | 4.1 | 3.647 | 3.744 | 2.918 | 2.838 | 4.221 |

TABLE III. Room-temperature experimental lattice constant $a_0$ in bohrs along with the experimental and theoretical direct-band-gap energies $E_g$ in eV of the semiconductors studied in this paper with SOC. For the indirect semiconductors, we only report the direct gap. We mention that for InSb, GaSb, InAs, and Ge the notation "≈0" means that the theoretical gaps are of the order of $≈10^{-11}$ eV.

| | $a_0$ | $E_g$ | | | |
| | | Expt. | LDA-HGH | GGA-HGH | mGGA-HGH |
|---|---|---|---|---|---|
| | | Direct semiconductors with SOC | | | |
| GaAs | 10.684 | 1.424 | 0.356 | 0.394 | 1.125 |
| InSb | 12.243 | 0.18 | ≈0 | ≈0 | 0.069 |
| GaSb | 11.519 | 0.75 | ≈0 | ≈0 | 0.385 |
| InAs | 11.448 | 0.345 | ≈0 | ≈0 | 0.412 |
| ZnS | 10.223 | 3.54 | 2.639 | 2.815 | 3.892 |
| ZnSe | 10.711 | 2.82 | 1.524 | 1.684 | 2.590 |
| CdTe | 12.24 | 1.5 | 0.732 | 0.869 | 1.493 |
| | | Indirect semiconductors with SOC | | | |
| Si | 10.26 | 3.4 | 2.515 | 2.569 | 2.843 |
| GaP | 10.3 | 2.78 | 1.785 | 1.838 | 2.714 |
| Diamond | 6.74 | 6.5 | 5.666 | 5.732 | 5.856 |
| Ge | 10.69 | 0.805 | ≈0 | ≈0 | 0.421 |
| BeTe | 10.61 | 4.1 | 3.297 | 3.393 | 3.892 |

Collecting the above results leads us to write the full 2PA susceptibility as

$$\chi^{abcd} = \chi_\omega^{abcd} + \chi_{2\omega}^{abcd},$$
(A47)

where

$$\chi_{p\omega}^{abcd} = \left( \chi_{1,1,p\omega}^{abcd} + \chi_{1,2,p\omega}^{abcd} + \chi_{1,3,p\omega}^{abcd} + \chi_{2,1,p\omega}^{abcd} + \chi_{2,2,p\omega}^{abcd} + \chi_{2,3,p\omega}^{abcd} + \chi_{3,1,p\omega}^{abcd} + \chi_{3,2,p\omega}^{abcd} + \chi_{3,3,1,p\omega}^{abcd} + \chi_{3,3,2,p\omega}^{abcd} \right.$$
$$\left. + \chi_{4,1,p\omega}^{abcd} + \chi_{4,2,p\omega}^{abcd} + \chi_{4,3,1,p\omega}^{abcd} + \chi_{4,3,2,p\omega}^{abcd} \right),$$
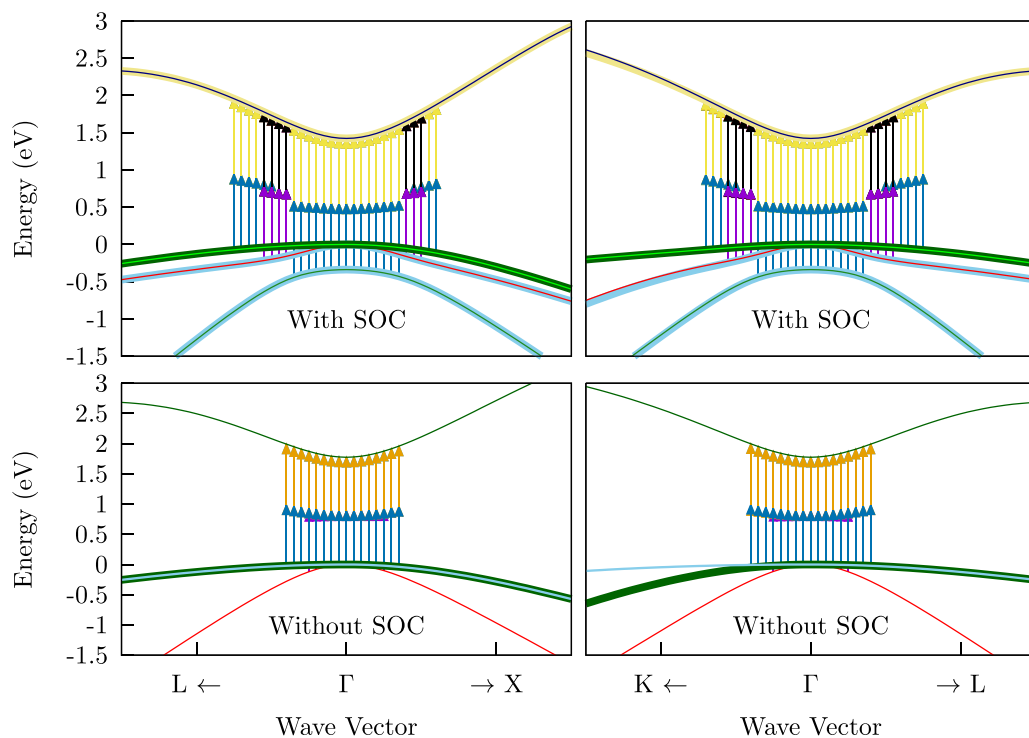(A48)



FIG. 15. Band structure of GaAs, where the arrows denote the corresponding $2\omega$ transitions that contribute to 2PA around $0.94 \pm 0.15$ eV where SOC is included (top panels), and around $0.93 \pm 0.15$ eV where SOC is not included (bottom panels). These energies correspond to the peak of the spectra shown in Fig 9. Each arrow represents the two $\omega$ photons that are absorbed, thus going from a valence band to a conduction band. See text for details.

with $p = 1, 2$. Using Fig. 1, we identify

$$\rho_{eii}^{(3)} = \chi_{21}^{(3)} + \chi_{22}^{(3)} + \chi_{11}^{(3)} + \chi_{12}^{(3)}, \tag{A49}$$

$$\rho_{eie}^{(3)} = \chi_{23}^{(3)} + \chi_{13}^{(3)}, \tag{A50}$$

$$\rho_{eei}^{(3)} = \chi_{32}^{(3)} + \chi_{42}^{(3)} + \chi_{31}^{(3)} + \chi_{42}^{(3)}, \tag{A51}$$

$$\rho_{eee}^{(3)} = \chi_{331}^{(3)} + \chi_{432}^{(3)} + \chi_{332}^{(3)} + \chi_{431}^{(3)}. \tag{A52}$$

## APPENDIX B: EXPERIMENTAL $a_0$ AND EXPERIMENTAL AND THEORETICAL $E_g$ VALUES AND ADDITIONAL RESULTS

In Tables II and III, we give the room-temperature experimental lattice constant $a_0$, in bohrs, along with the experimental and theoretical band-gap energies $E_g$, in eV, for the semiconductors studied in this paper, with and without SOC. For the indirect semiconductors, we only report the direct gap. It is worth mentioning that the mGGA-HGH scheme overestimates $E_g$ for InSb, InAs, ZnS, CdTe, and BeTe without SOC, and only for InAs and ZnS with SOC; this could be due to the fact that we are using room-temperature lattice constants instead of 0-K values. In Fig. 14, we show a full view of the band structure of Si along with the 2PA arrows around $2.2 \pm 0.15$ eV, and in Fig. 15, we show the band structure for GaAs around $0.94 \pm 0.15$ and $0.93 \pm 0.15$ eV, corresponding to the peak energies of the spectra in Fig. 9 (the former is when SOC is included, and the latter is when SOC is not included). The spin-split bands are very well seen in the top panels of Fig. 15. For these energies, the only transitions that contribute to $\beta_{11}^{\parallel}(\omega)$ are from $v = 1, 2, 3$ to $c = 1$.

In Fig. 16, we show a comparison of the 2PA coefficient $\beta_{11}^{\parallel}(\omega)$ and $\text{Im}[\chi_{aa}(\omega)]$ (whose abscissa is rescaled by $\hbar\omega/2$) for GaAs, Si, and GaP. We see that although for Si and GaP $\beta_{11}^{\parallel}(\omega)$ and $\text{Im}[\chi_{aa}(\omega)]$ resemble each other only up to the first resonance, for GaAs there is no resemblance for most of the 2PA photon energies, and they only resemble each other just around $E_{\text{expt}}$, where 2PA would compete with the linear absorption and thus is not interesting for 2PA. Also, except for the Si resonance of $\sim 2.6$ eV, we do not find a clear and compelling correlation between $\beta_{11}^{\parallel}(\omega)$ and $\text{Im}[\chi_{aa}(\omega)]$.

In Fig. 17, we show the spectra of the 2PA coefficient $\beta_{11}^{\parallel}(\omega)$ of several direct and indirect semiconductors, where the direct-band-gap $E_g$ is used in the calculation. We show the spectra for energies $E_g/2 \leqslant \hbar\omega < E_g$, where only 2PA is present, and thus the linear absorption does not intervene. The $\beta_{11}^{\parallel}(\omega)$ obtained for the different semiconductors is arranged from the semiconductor with the highest value (InSb) to the semiconductor with the lowest value (ZnSe). It is worth mentioning that the 2PA energy range spans from $\sim 0.1$ for InSb to $\sim 6.5$ eV for diamond, and the intensity in $\text{mW}^{-1} \times 10^{-8}$ goes from $\sim 0.4$ for ZnS to $\sim 70$ for InSb. It should be clear that the particular characteristic of every material determines the spectral range of absorption and intensity. Moreover, the

spectroscopy 2PA line shape depends on the electron dynamics, mainly that of the electrons in the last valence and first conduction bands, as explained in the main text.
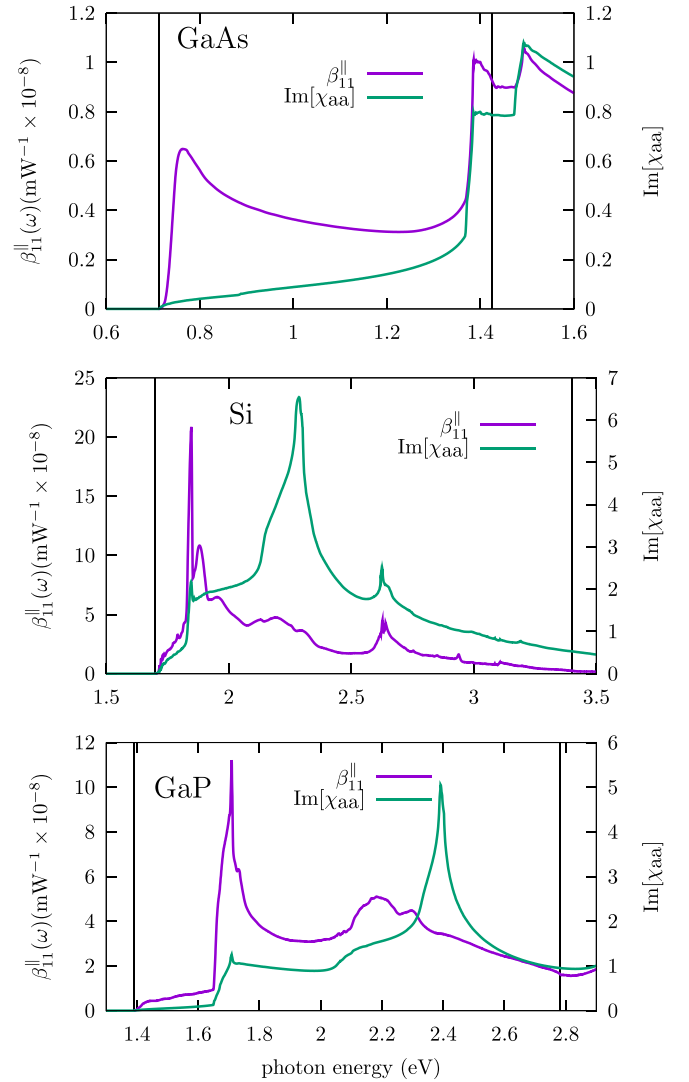


FIG. 16. 2PA $\beta_{11}^{\parallel}(\omega)$ coefficient and $\text{Im}[\chi_{aa}(\omega)]$ (whose abscissa is rescaled by $\hbar\omega/2$) for GaAs, Si, and GaP. The left vertical lines are at $E_{\text{expt}}/2$ whereas the right vertical lines are at $E_{\text{expt}}$ of the corresponding material. See text for details.
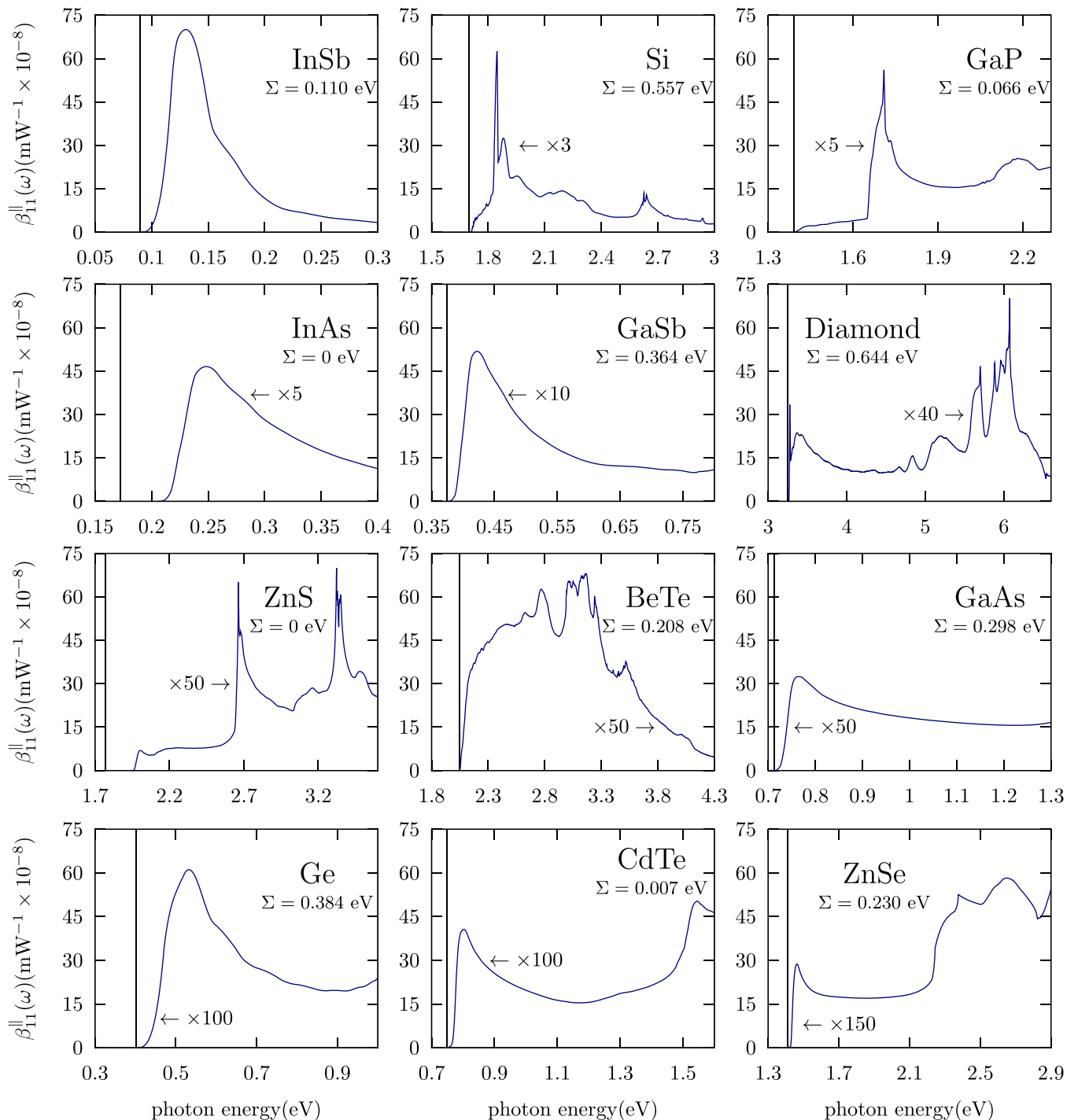
FIG. 17. 2PA $\beta_{11}^{\parallel}(\omega)$ coefficient of Eq. (44) for several semiconductors as a function of photon energy $\hbar\omega$. The materials are oriented along the (110) crystallographic direction, and the incident beam is polarized in the (100) direction. The scissors correction $\Sigma$ (in eV) is shown for each material. The vertical black line is at $E_{\text{expt}}/2$. All the spectra are calculated with mGGA-HGH including SOC.

[1] M. Göppert-Mayer, Ann. Phys. (Berlin) **401**, 273 (1931).

[2] W. Denk, J. H. Strickler, and W. W. Webb, Science **248**, 73 (1990).

[3] E.-S. Wu, J. H. Strickler, W. R. Harrell, and W. W. Webb, in *Optical/Laser Microlithography V*, edited by J. D. Cuthbert,

Proceedings of SPIE Vol. 1674 (SPIE, Bellingham, WA, 1992), pp. 776–782.

[4] S. Maruo, O. Nakamura, and S. Kawata, Opt. Lett. **22**, 132 (1997).

[5] S. Kawata, H. Sun, T. Tanaka, and K. Takada, Nature (London) **412**, 697 (2001).

[6] L. W. Tutt and T. F. Boggess, Prog. Quantum Electron. **17**, 299 (1993).

[7] D. A. Parthenopoulos and P. M. Rentzepis, Science **245**, 843 (1989).

[8] K. Ogawa, Appl. Sci. **4**, 1 (2014).

[9] J. Schmitt, V. Heitz, A. Sour, F. Bolze, H. Ftouni, J.-F. Nicoud, L. Flamigni, and B. Ventura, Angew. Chem., Int. Ed. **54**, 169 (2015).

[10] B. J. Furey, B. J. Stacy, T. Shah, R. M. Barba-Barba, R. Carriles, A. Bernal, B. S. Mendoza, B. A. Korgel, and M. C. Downer, ACS Nano **16**, 6023 (2022).

[11] K. Wei, Z. Xu, R. Chen, X. Zheng, X. Cheng, and T. Jiang, Opt. Lett. **41**, 3821 (2016).

[12] T. Ogawa and Y. Kanemitsu, *Optical Properties of Low-Dimensional Materials* (World Scientific, Singapore, 1996).

[13] B. J. Furey, R. M. Barba-Barba, R. Carriles, A. Bernal, B. S. Mendoza, and M. C. Downer, J. Appl. Phys. **129**, 183109 (2021).

[14] D. C. Hutchings and E. W. Van Stryland, J. Opt. Soc. Am. B **9**, 2065 (1992).

[15] C. Aversa, J. E. Sipe, M. Sheik-Bahae, and E. W. Van Stryland, Phys. Rev. B **50**, 18073 (1994).

[16] D. C. Hutchings and B. S. Wherrett, J. Mod. Opt. **41**, 1141 (1994).

[17] D. C. Hutchings and B. S. Wherrett, Phys. Rev. B **49**, 2418 (1994).

[18] C. Aversa and J. E. Sipe, Phys. Rev. B **52**, 14636 (1995).

[19] J. L. P. Hughes and J. E. Sipe, Phys. Rev. B **53**, 10751 (1996).

[20] M. Murayama and T. Nakayama, Phys. Rev. B **49**, 5737 (1994).

[21] M. Murayama and T. Nakayama, Phys. Rev. B **52**, 4986 (1995).

[22] M. Murayama and T. Nakayama, Phys. Rev. B **55**, 9628 (1997).

[23] W.-R. Hannes and T. Meier, Phys. Rev. B **99**, 125301 (2019).

[24] D. J. Passos, G. B. Ventura, J. M. B. Lopes dos Santos, and J. M. Viana Parente Lopes, J. Phys.: Condens. Matter **33**, 465701 (2021).

[25] Indeed, the factor of 3 arises from the sum over the allowed frequency permutations as obtained from Eq. (3).

[26] G. Onida, L. Reining, and A. Rubio, Rev. Mod. Phys. **74**, 601 (2002).

[27] S. M. Anderson, N. Tancogne-Dejean, B. S. Mendoza, and V. Véniard, Phys. Rev. B **91**, 075302 (2015).

[28] E. N. Adams, J. Chem. Phys. **21**, 2013 (1953).

[29] E. I. Blount, in *Solid State Physics*, edited by F. Seitz, and D. Turnbull, Solid State Physics Vol. 13 (Elsevier, New York, 1962), p. 305.

[30] B. S. Mendoza and W. L. Mochán, J. Opt. Soc. Am. B **38**, 1918 (2021).

[31] J. L. Cabellos, B. S. Mendoza, M. A. Escobar, F. Nastos, and J. E. Sipe, Phys. Rev. B **80**, 155205 (2009).

[32] The ABINIT code is a common project of the Universitè Catholique de Louvain, Corning Incorporated, and other contributors [44]; X. Gonze, B. Amadon, G. Antonius, F. Arnardi, L. Baguet, J.-M. Beuken, J. Bieder, F. Bottin, J. Bouchet, E. Bousquet, N. Brouwer, F. Bruneval, G. Brunin, T. Cavignac, J.-B. Charraud, W. Chen, M. Côté, S. Cottenier, J. Denier, G. Geneste *et al.*, Comput. Phys. Commun., **248**, 107042 (2020); A. H. Romero, D. C. Allan, B. Amadon, G. Antonius, T. Applencourt, L. Baguet, J. Bieder, F. Bottin, J. Bouchet, E. Bousquet, F. Bruneval, G. Brunin, D. Caliste, M. Côté, J. Denier, C. Dreyer, P. Ghosez, M. Giantomassi, Y. Gillet, O. Gingras *et al.*, J. Chem. Phys., **152**, 124102 (2020).

[33] N. Troullier and J. L. Martins, Phys. Rev. B **43**, 1993 (1991).

[34] L. Kleinman and D. M. Bylander, Phys. Rev. Lett. **48**, 1425 (1982).

[35] C. Hartwigsen, S. Goedecker, and J. Hutter, Phys. Rev. B **58**, 3641 (1998).

[36] J. P. Perdew, Phys. Rev. B **33**, 8822 (1986).

[37] G. Ortiz and P. Ballone, Phys. Rev. B **50**, 1391 (1994); **56**, 9970(E) (1997).

[38] E. Räsänen, S. Pittalis, and C. R. Proetto, J. Chem. Phys. **132**, 044112 (2010).

[39] F. Nastos, J. Rioux, M. Strimas-Mackey, B. S. Mendoza, and J. E. Sipe, Phys. Rev. B **76**, 205113 (2007).

[40] D. H. Reitze, T. R. Zhang, W. M. Wood, and M. C. Downer, J. Opt. Soc. Am. B **7**, 84 (1990).

[41] M. Dvorak, W. Schroeder, D. Andersen, A. Smirl, and B. Wherrett, IEEE J. Quantum Electron. **30**, 256 (1994).

[42] S. M. Anderson, B. S. Mendoza, G. Fugallo, and F. Sottile, Phys. Rev. B **100**, 045205 (2019).

[43] M. J. Lax, *Symmetry Principles in Solid State and Molecular Physics* (Wiley, New York, 1974).

[44] https://www.abinit.org.